Supporting information for

# Nitrogen Fixation via a Terminal Fe(IV) Nitride

Niklas B. Thompson,[†] Michael T. Green,[‡] Jonas C. Peters[†]

[†]Division of Chemistry and Chemical Engineering, California Institute of Technology, Pasadena, California 91125, USA

[‡]Department of Chemistry, University of California – Irvine, Irvine, California 92697, USA

**Table of Contents:**

**Experimental and Synthetic Details**

Unless noted otherwise, all manipulations were carried out using standard Schlenk or glovebox techniques under an $N_2$ atmosphere. Solvents were deoxygenated and dried by thoroughly sparging with $N_2$ followed by passage through an activated alumina column in a solvent purification system by SG Water, USA LLC. Deoxygenated, anhydrous 2-methyltetrahydrofuran (2-MeTHF) was purified by stirring over sodium-potassium alloy and filtering through a short column of activated alumina prior to use. Nonhalogenated solvents were tested with sodium benzophenone ketyl in tetrahydrofuran (THF) in order to confirm the absence of oxygen and water. Deuterated solvents were purchased from Cambridge Isotope Laboratories, Inc., degassed, and dried over activated 3 Å molecular sieves prior to use.

The compounds tris(*o*-diisopropylphosphinophenyl)borane ($P_3^B$),[1] ($P_3^B$)Fe(Br),[2] ($P_3^B$)Fe(Me),[3] [Na($Et_2O$)$_2$][($P_3^B$)Fe($N_2$)],[2] [Na(12-crown-4)$_2$][($P_3^B$)Fe($N_2$)],[2] [H($OEt_2$)$_2$][$BAr^F_4$] ($HBAr^F_4$),[4] and $^{57}FeCl_2$,[5] were prepared according to literature procedures. $^{57}$Fe-labelled [Na(12-crown-4)$_2$][($P_3^B$)Fe($N_2$)] was prepared as usual, but using ($P_3^B$)$^{57}$Fe(Cl) as the precursor. ($P_3^B$)$^{57}$Fe(Cl) was prepared by a synthesis analogous to that of the bromide analog, but replacing $FeBr_2$ with $^{57}FeCl_2$ as the Fe precursor. All other reagents were purchased from commercial vendors and used without further purification unless otherwise stated.

NMR Spectroscopy

Chemical shifts for $^1$H and $^{13}$C are reported in ppm relative to tetramethylsilane, using resonances from residual solvent as internal standards; $^{31}$P and $^{11}$B resonances are reported in ppm, referenced to the signal of the deuterated solvent used to lock the instrument.

IR Spectroscopy

IR measurements were obtained as powders or thin films formed by evaporation of solutions using a Bruker Alpha Platinum ATR spectrometer with OPUS software.

UV-Visible Spectroscopy

Optical spectroscopy measurements were collected with a Cary 50 UV-vis spectrophotometer using a 1-cm two-window quartz cell.

Electrochemistry

Cyclic voltammetry measurements were carried out in a glovebox under an $N_2$ atmosphere in a one-compartment cell using a CH Instruments 600B electrochemical analyzer. A glassy carbon electrode was used as the working electrode and a carbon rod was used as the auxiliary electrode. The reference electrode was AgOTf/Ag in THF isolated by a CoralPor™ frit (obtained from BASi). The ferrocenium/ferrocene couple ($Fc^+$/Fc) was used as an external reference. THF solutions of electrolyte (0.1 M [$NBu_4$][$PF_6$]) and analyte were also prepared under an inert atmosphere.

X-ray Crystallography

X-ray diffraction studies were carried out at the Caltech Division of Chemistry and Chemical Engineering X-ray Crystallography Facility using a dual source Bruker D8

Venture, four-circle diffractometer with a PHOTON CMOS detector. Data was collected at 100K using Mo Kα radiation (λ = 0.71073 Å). The crystals were mounted on a glass fiber under Paratone N oil. Structures were solved using SHELXT[6] and refined against $F^2$ on all data by full-matrix least squares with SHELXL.[7] All non-hydrogen atoms were refined anisotropically. All hydrogen atoms were placed at geometrically calculated positions and refined using a riding model. The isotropic displacement parameters of all hydrogen atoms were fixed at 1.2 (1.5 for methyl groups) times the $U_{eq}$ of the atoms to which they are bonded.

$^{57}$Fe Mössbauer Spectroscopy

Mössbauer spectra were recorded on a spectrometer from SEE Co. (Edina, MN) operating in the constant acceleration mode in a transmission geometry. The sample was kept in an SVT-400 cryostat form Janis (Wilmington, MA), using liquid He as a cryogen for temperatures below 80 K, and liquid $N_2$ as a cryogen for 80 K measurements. The quoted isomer shifts are relative to the centroid of the spectrum of a metallic foil of α-Fe at room temperature. Solid samples were prepared by grinding solid material into a fine powder and then mounted in to a Delrin cup fitted with a screw-cap as a boron nitride pellet. Solution samples were transferred to a sample cup and chilled to 77 K inside of the glovebox, and quickly removed from the glovebox and immersed in liquid $N_2$ until mounted in the cryostat. Data analysis was performed using version 4 of the program WMOSS (www.wmoss.org) and quadrupole doublets were fit to Lorentzian lineshapes.[8]

X-ray Absorption Spectroscopy (XAS)

Samples for XAS measurements were prepared in modified Mössbauer sample cups in which the bottom of the Delrin cup was removed and sealed with Kapton tape. All samples thus prepared were analyzed by Mössbauer spectroscopy at 80 K prior to collection of XAS data. Samples were maintained at temperatures of 80 K and below at all times.

XAS data collection was conducted at the Stanford Synchrotron Radiation Laboratory (SSRL) with the SPEAR 3 storage ring containing 500 mA at 3.0 GeV. Fe K-edge data were collected on the beamline 9-3 operating with a wiggler field of 2 T and employing a Si(220) double-crystal monochromator. Beamline 9-3 is equipped with a rhodium-coated vertical collimating mirror upstream of the monochromator and a bent-cylindrical focusing mirror (also rhodium-coated) downstream of the monochromator. Harmonic rejection was accomplished by setting the energy cutoff angle of the mirrors to 10 keV. The incident and transmitted X-ray intensities were monitored using nitrogen-filled ionization chambers, and for dilute samples X-ray absorption was monitored by measuring the Fe Kα fluorescence intensity using an array of 100 Canberra germanium detectors. For concentrated samples (≥ 10 mM), fluorescence was measured using a single-channel PIPS detector. During data collection, samples were maintained at a temperature of approximately 10 K using an Oxford instruments liquid helium flow cryostat. The energy was calibrated by reference to the absorption of a standard iron metal foil measured simultaneously with each scan, assuming a lowest energy inflection point of the iron foil to be 7111.3 eV. Samples were monitored for photodamage by comparing the pre-edge region between consecutive scans. In cases where photodamage was detected, the sample was moved to a previously un-exposed region and single scans

were collected; in this fashion, six first scans could be collected and integrated for each sample.

The raw XAS data were analyzed using the EXAFSPAK suite of programs.[9] Data were calibrated to the first inflection of the iron foil reference and averaged over all first scans for each sample. The edge region was background corrected by fitting a Gaussian function through the pre-edge region and subtracting this from the entire spectrum. A four-segment fourth-order spline was fit to the EXAFS region, and the spectrum was normalized to the edge jump. In most cases, a monochromator glitch at $k \approx 12$ Å$^{-1}$ was removed by fitting a cubic polynomial to the raw data. For dilute samples, a step at the Co K-edge (7709 eV) due to a small Co impurity detected in the incident X-rays was observed; note that since the step was present in the incident channel, the impurity was due to Co on the slits which focus the X-rays on the sample, not in the sample itself. This impurity was corrected by fitting a fourth-order polynomial through the step in the raw data to determine a constant offset, which was subsequently subtracted from the data after the step. Interatomic distances obtained from simulation of the raw, uncorrected EXAFS data were found to be identical to those obtained from simulation of the data deglitched in this manner (*vide infra*). No smoothing, filtering, or related operations were performed on the data. The pre-edge region was fit between 7108 and 7119 eV using the EDG_FIT utility. Resonances were fit with pseudo-Voigt lineshapes, where the weight of the Lorentzian and Gaussian components were allowed to refine freely. The EXAFS oscillations $\chi(k)$ were quantitatively analyzed by non-linear least square curve-fitting. The $k^3$-weighted data were fit from $k = 3$–15 Å$^{-1}$. *Ab initio* theoretical phase and amplitude functions were calculated using the program FEFF version 7.[10]

Synthetic Details

**Synthesis of $[(P_3^B)FeN_2]^{2-}$: *From $[Na(Et_2O)_2][(P_3^B)Fe(N_2)]$.*** A solution of $[Na(Et_2O)_2][(P_3^B)Fe(N_2)]$ in THF (7 mM) was passed iteratively 3 times through a short column of $KC_8$ (~ 0.7 × 0.7 mm) packed on top of a glass microfiber filter. An aliquot of this solution was dried to a thin film on the sample plate of an ATR-IR spectrometer. The resultant IR spectrum displays an intense vibration at 1803 cm$^{-1}$ attributable to the N–N vibration of $[(P_3^B)FeN_2]^{2-}$ (Fig. S12). The difference in $N_2$ stretching frequencies between $[(P_3^B)FeN_2]^{2-}$ produced from reduction of $[Na(Et_2O)_2][(P_3^B)Fe(N_2)]$ and $[(P_3^B)FeN_2]^{2-}$ produced from reduction of $[Na(12\text{-crown-}4)_2][(P_3^B)Fe(N_2)]$ ($\Delta\nu_{NN} = 31$ cm$^{-1}$, *vide infra*) is nearly identical to that observed for $[Na(12\text{-crown-}4)_2][(P_3^B)Fe(N_2)]$ versus $[Na(Et_2O)_2][(P_3^B)Fe(N_2)]$ ($\Delta\nu_{NN} = 29$ cm$^{-1}$), suggesting coordination of $Na^+$ to the $N_2$ ligand of $[(P_3^B)FeN_2]^{2-}$ produced *in situ* from $[Na(Et_2O)_2][(P_3^B)Fe(N_2)]$.

***From $[Na(12\text{-crown-}4)_2][(P_3^B)Fe(N_2)]$.*** A solution of $[Na(12\text{-crown-}4)_2][(P_3^B)Fe(N_2)]$ in DME (1 to 10 mM) was similarly reduced via iterative passage through a column of $KC_8$. The filtered supernatant was layered with an equal volume of $Et_2O$ and placed in a freezer at −35 °C. After ca. 24 hrs, the mother liquor was decanted off of black crystalline solids, which were liberally washed with $Et_2O$ before drying *in vacuo*. The solid state IR spectrum shows an intense resonance at 1836 cm$^{-1}$ attributable to the N–N vibration of $[Na(12\text{-crown-}4)][K(DME)_x][(P_3^B)Fe(N_2)]$. For NMR analysis, deuterated THF was employed as the solvent, and the filtered black solution was sealed in an NMR tube fitted with a J-Young adapter containing a spatula tip of $KC_8$. Based on the NMR data, $[(P_3^B)FeN_2]^{2-}$ maintains $C_3$ symmetry in solution, with a single set of

aromatic resonances in the $^{1}$H spectrum, and one singlet in the $^{31}$P spectrum. As $[(P_3^B)Fe(N_2)]^{2-}$ (−3.2 V vs $Fc^+/Fc$) is more reducing than its alkali metal counterions (e.g. −3.04 V vs $Fc^+/Fc$ for $Na^{+/0}$) in ethereal solvents, it is subject to disproportionation in solution, and such preparations invariably contain $[K(DME)_x][(P_3^B)Fe(N_2)]$ as a contaminant ($\nu_{NN}$ = 1893 $cm^{-1}$). Thus elemental analysis was not collected. For Mössbauer studies, $^{57}$Fe-enriched $[Na(12\text{-crown-4})][K(Solv)_x][(P_3^B)FeN_2]$ was prepared in situ from 100% $^{57}$Fe-enriched $[Na(12\text{-crown-4})][(P_3^B)FeN_2]$ using the same method with THF or 2-MeTHF as the solvent, and the filtered solution was immediately frozen into a Delrin sample holder.

$^{1}$H NMR (400 MHz, *d*$_8$-THF, 293 K, ppm): δ 7.14 (d, *J* = 5 Hz, Ar-C*H*, 3H) , 6.84 (d, *J* = 5 Hz, Ar-C*H*, 3H), 6.45 (t, *J* = 6.5 Hz, Ar-C*H*, 3H), 6.29 (t, *J* = 6.5 Hz, Ar-C*H*, 3H), 3.61 (br, 12-crown-4), 3.59 (br, THF), 2.35 (br, -C*H*$(CH_3)_2$, 6H), 1.78 (br, -CH(C*H*$_3$)), 1.73 (br, THF); N.B., accurate integrations for the isopropyl methyl protons of the ligand and the methylene protons of the $[(12\text{-crown-4})_2Na]^+$ ion could not be obtained due to overlap with the residual THF resonances appearing at 1.73 and 3.59 ppm. $^{31}$P{$^{1}$H} (162 MHz, $C_6D_6$, 293 K, ppm): δ 79.65.

**Synthesis of $(P_3^B)Fe(NNMe_2)$:** To a suspension of $(P_3^B)FeBr$ (200 mg, 0.275 mmol) in 5.5 mL $Et_2O$ was added MeOTf (65 μL, 0.578 mmol), and the mixture was subsequently cooled to −78 °C with stirring in the cold well of an $N_2$-filled glove box. A scintillation vial containing $KC_8$ (123 mg, 0.909 mmol) suspended in 2.5 mL $Et_2O$ was similarly chilled, and then transferred to the stirring $(P_3^B)FeBr$/MeOTf mixture via pipette; this vial was additionally washed with 1 mL of pre-chilled $Et_2O$, which was subsequently added to the reaction mixture. The mixture was allowed to stir at −78 °C for 1 hr, and then allowed to warm to room temperature and stirred an additional 3 hrs. The solvent was removed *in vacuo*, and the remaining solids extracted with pentane and filtered over a pad of celite until the filtrate, containing crude product, is colorless (ca. 50 mL). The filtrate was concentrated to dryness, and THF (ca. 5 mL) and 0.7 wt% Na(Hg) (1.375 mmol $Na^0$) were added. This mixture is stirred rapidly overnight (ca. 12 hrs), at which point the dark solution is decanted from the excess Na(Hg), the solvent removed *in vacuo*, and the remaining solids extracted with pentane and filtered through a celite pad until the filtrate runs colorless. The pentane extract is concentrated to ca. 5 mL and then cooled to −35 °C. After 2 days, the mother liquor is decanted, the remaining solids washed with cold pentane (5 × 1 mL), and dried *in vacuo* to yield $(P_3^B)Fe(NNMe_2)$ as dark brown crystals (24 mg, 13%). Crystals suitable for XRD were obtained by slow evaporation of a pentane solution of $(P_3^B)Fe(NNMe_2)$ at room temperature.

$^{1}$H NMR (400 MHz, $C_6D_6$, 293 K, ppm): δ 9.73 (d, *J* = 7 Hz, Ar-C*H*, 3H) , 8.19 (t, *J* = 7 Hz, Ar-C*H*, 3H), 6.97 (d, *J* = 7 Hz, Ar-C*H*, 3H), 5.40 (t, *J* = 7 Hz, Ar-C*H*, 3H), 5.29 (br, -C*H*$(CH_3)_2$, 3H), 4.06 (br, -C*H*$(CH_3)_2$, 3H), 1.11 (d, *J* = 6 Hz, -CH(C*H*$_3$), 9H), 0.95 (d, *J* = 6 Hz, -CH(C*H*$_3$), 9H), 0.64 (d, *J* = 6 Hz, -CH(C*H*$_3$), 9H), 0.06 (d, *J* = 6 Hz, -CH(C*H*$_3$), 9H), −18.66 (br, -NN(C*H*$_3$)$_2$, 6H). $^{13}$C{$^{1}$H} NMR (101 MHz, $C_6D_6$, 293 K, ppm): δ 241.88 (Ar-C), 137.78 (Ar-*C*H), 120.34 (Ar-*C*H), 119.28 (Ar-*C*H), 75.39 (Ar-*C*), 62.24 (Ar-*C*H), 45.38 (-*C*H$(CH_3)_2$), 33.56 (-CH(*C*H$_3$)), 22.62 (-CH(*C*H$_3$)), 17.67 (-CH(*C*H$_3$)), 16.92 (-CH(*C*H$_3$)), −10.74 (-*C*H$(CH_3)_2$); N.B., a resonance for the *N*-methyl carbon atom could not be located in the chemical shift range from 1000 to −500 ppm, even by $^{1}$H-detected HSQC/HMQC. The resonance is likely too broad at 293 K by

exchange with the paramagnetic excited state to be observed (*vide infra*). $^{31}P\{^{1}H\}$ (162 MHz, $C_6D_6$, 293 K, ppm): δ 806.61 (br, FWHM = 2741 Hz). $^{11}B$ (128 MHz, $C_6D_6$, 293 K, ppm) δ −396.23 (br, FWHM = 909 Hz). UV-Visible (toluene, 293 K, nm {ε, $cm^{-1}$ $M^{-1}$}): 551 {636}, 774 {139}. Anal. Calc. for $C_{38}H_{60}BFeN_2P_3$: C, 64.79; H, 8.58; N, 3.98. Found: C, 65.06; H, 8.56; N, 3.70.

**Synthesis of $(P_3^B)$Fe(OTf):** A suspension of $(P_3^B)$Fe(Me) (25 mg, 0.038 mmol) in 1 mL of $Et_2O$ was chilled to −78 °C in the cold well of an $N_2$ filled glove box. A similarly chilled solution of TfOH (3.5 mL, 0.040 mmol) in 1 mL of $Et_2O$ was added dropwise to the suspension of $(P_3^B)$Fe(Me), and the resultant mixture was removed from the cold well and allowed to warm to room temperature with stirring over the course of 1 hour. The solvent was removed *in vacuo*, and the remaining brown-green solids were extracted with pentane (3 × 15 mL) and filtered through a pad of celite. The filtrate was dried *in vacuo* to yield analytically pure $(P_3^B)$Fe(OTf) as a yellow-green powder (25 mg, 83%). Crystals suitable for XRD were grown by slow evaporation of a pentane solution of $(P_3^B)$Fe(OTf) at room temperature.

$^{1}H$ NMR (400 MHz, $C_6D_6$, 293 K, ppm): δ 57.27, 35.29, 26.52, 24.70, 5.32, 4.38, 2.93, 0.86, -3.15, -26.04. $\mu_{eff}$ ($C_6D_6$, Evans method, 293 K): 4.1 $\mu_B$. UV-Visible (2-MeTHF, 293 K, nm {ε, $cm^{-1}$ $M^{-1}$}): 562 {126}, 749 {124}. Anal. Calc. for $C_{37}H_{54}BF_3FeO_3P_3S$: C, 55.87; H, 6.84. Found: C, 55.78; H, 6.76.

Protonation studies of $[(P_3^B)FeN_2]^{2-}$

**Using TfOH:** As described above, a solution of $[(P_3^B)FeN_2]^{2-}$ (0.0028 mmol) in 500 μL 2-MeTHF was prepared *in situ* from $^{57}$Fe-labelled $[Na(12\text{-crown-}4)_2][(P_3^B)Fe(N_2)]$, and immediately transferred to a Mössbauer or XAS sample holder and glassed (91 K) in the cold well of an $N_2$ filled glove box chilled to 77 K. A solution of TfOH in 2-MeTHF (200 μL 80 mM, 0.016 mmol, 6 equiv) was layered on top and allowed to form a glass (final [Fe] = 4 mM, final [TfOH] = 24 mM). Using pre-chilled stainless steel forceps, the sample cup was lifted off of the bottom of the cold well, and the mixture was allowed to de-glass. A pre-chilled stainless steel stir rod was used to mix the viscous, supercooled 2-MeTHF briefly before replacing the cup on the bottom of the well and allowing the solvent to re-glass. This procedure was repeated until the desired mixing time was reached, at which point the sample was allowed to re-glass on the bottom of the cold well before it was transferred quickly out of the glovebox and stored at 77 K prior to analysis.

N.B., at early reaction times (< 15 min. of mixing) it is critical that temperature be maintained low enough that the 2-MeTHF appears as a very viscous gel. However, with enough reaction time, the mixture occasionally flash-freezes (typically after about 20 min. of mixing), at which point the frozen mixture must be carefully thawed to 137 K before re-glassing and repeating the above procedure.

**Using $HBAr^F_4$:** The procedure is identical to that using TfOH, but $HBAr^F_4$ was used as the proton source (58 mg, 0.057 mmol, 20 equiv).

Protonation of $[Na(12\text{-crown-}4)_2][(P_3^B)Fe(N_2)]$

The procedure use was identical to that described above for protonation of $[(P_3^B)FeN_2]^{2-}$, with the following changes: $[(P_3^B)FeN_2]^{2-}$ was replaced with $^{57}$Fe-labelled

[Na(12-crown-4)$_2$][($P_3^B$)Fe($N_2$)] (2.0 mg, 0.0019 mmol); 15 equiv of TfOH was used (2.5 μL, 0.028 mmol); and the total reaction volume was 500 μl (final [Fe] = 4 mM). This mixture was stirred for 15 min. before re-glassing and collecting Mössbauer spectra.

Studies with $NH_3/N_2H_4$ quantification:

Protonation of [($P_3^B$)Fe$N_2$]$^{2-}$ or [Na(12-crown-4)$_2$][($P_3^B$)Fe($N_2$)] with TfOH was carried out as described above, but in a 20 mL scintillation vial, on larger scale (0.0095 mmol Fe, [Fe] = 4 mM), and with a higher concentration of TfOH (80 mM, 20 equiv). The reaction was mixed for 30 min. at T ≤ 137 K. (Mössbauer experiments under identical conditions shows that the yield of [($P_3$B)Fe≡N]$^+$ is typically ~ 50%; see Fig. S24.) At this point, a stir bar was added to the mixture, which was allowed to warm to room temperature with stirring over the course of 15 min. The warmed solution was then transferred to Schlenk tube and refrozen in the liq. $N_2$ chilled cold well before a solution of NaO*t*Bu (37 mg, 0.38 mmol) in 1 mL THF was added and frozen on top of the reaction mixture. The Schlenk tube was sealed and thawed to room temperature with stirring over the course of 15 min. At this point, the Schlenk tube was removed from the $N_2$-filled glove box, the volatiles vacuum-transferred onto an excess of 2.0 M HCl in $Et_2O$ and analyzed for [$NH_4$][Cl] and [$N_2H_6$][Cl]$_2$ as described previously.[4]

For experiments in which reductant was added after initial protonation of [($P_3^B$)Fe$N_2$]$^{2-}$, an identical procedure was used, with the following modification. After mixing [($P_3^B$)Fe$N_2$]$^{2-}$ and TfOH in supercooled 2-MeTHF for 30 min., the solution was re-glassed, and a solution of CoCp*$_2$ in 2-MeTHF (31 mg, 0.095 mmol, 10 equiv) was layered on top and allowed to glass. The mixture was mechanically stirred at T ≤ 137 K for an additional 30 min. At this point, a stir bar was added to the mixture, which was allowed to warm to room temperature with stirring over the course of 15 min. The reaction was subsequently worked up as described above.

The following procedure was employed for a catalytic reaction: In a nitrogen-filled glovebox, a stock solution of [($P_3^B$)Fe][$BAr^F_4$] in $Et_2O$ was prepared. An aliquot of this stock solution (2.3 μmol) was added to a Schlenk tube and evaporated to dryness under vacuum, depositing a film of [($P_3^B$)Fe][$BAr^F_4$]. The tube was then charged with a stir bar and cooled to 77 K in a cold well. To the cold tube was added solid Cp*$_2$Co (0.124 mmol, 54 equiv) and a solution of TfOH in $Et_2O$ (0.247 mmol, 107 equiv). The final volume of solvent was 1 mL. This solution was allowed to cool and freeze for 5 minutes. The temperature of the system was allowed to equilibrate for 5 minutes and then the tube was sealed with a Teflon screw-valve. This tube was passed out of the box into a liquid $N_2$ bath and transported to a fume hood. The tube was then transferred to a dry ice/acetone bath where was thawed and allowed to stir at 195 K for 3 hrs. At this point the tube was warmed to room temperature with stirring, and stirred at room temperature for 5 minutes. The reaction was subsequently worked up and quantified for the presence of $NH_3/N_2H_4$ as described above.

The results of these experiments are tabulated in Table S11. (N.B., during vacuum transfer the temperature of the system was maintained at 298 K and below to prevent decomposition of $N_2H_4$.)

Computational Methods

All calculations were carried out using version 3.0.3 of the ORCA package.[11] Given the experimentally measured structure and ground state/excited state energy splitting for ($P_3^B$)Fe($NNMe_2$) (*vide infra*), this was used as a model for testing the pure exchange-correlation functionals BP86,[12] M06-L,[13] and TPSS.[14] For the purposes of testing, gas-phase geometry optimizations were carried out using the def2-SVP(C,H)/def2-TZVP basis set (with atomic coordinates from XRD as inputs),[15] followed by a frequency calculation at the same level of theory to ensure a true minimum. Calculations employed a fine integration grid (ORCA Grid5) during geometry optimization, as well as during the final single-point calculation (Grid6). The importance of relativistic effects were tested by inclusion of the zeroth order regular approximation (ZORA) with the BP86 functional,[16] using the scalar relativistically-recontracted def2-ZORA-SVP(C,H)/def2-ZORA-TZVP basis sets and def2-SVP(C,H)/def2-TZVP auxiliary basis sets.[17] The results of these calculations are collected in Table S13 and S14, from which it can be seen that the ZORA-BP86 method produces the most accurate geometry, as well as a singlet-triplet $\Delta H$ that agrees well with the experimental value. All subsequent geometry optimizations and single-point energy calculations employed this method.

For the calculation of Mössbauer parameters, the hybrid functional TPSSh[18] was used with the def2-SVP(C,H)/def2-TZVP basis set on all non-Fe atoms and the "core properties" CP(PPP) basis set for Fe.[19] The angular integration grid was set to Grid4 (NoFinalGrid), with increased radial accuracy for the Fe atom (IntAcc 7). To simulate solid state effects, a continuum solvation model was included (COSMO) with a solvent of intermediate dielectric (methanol). To calibrate the isomer shift scale and estimate the error in the calculated quadrupole splitting using this method, the Mössbauer parameters of 8 ($P_3^B$)Fe complexes were computed from crystallographically-determined structures; in addition, the parameters of the previously-characterized nitrido complex ($PhBP_3^{iPr}$)Fe≡N were computed using coordinates from the ZORA-BP86 method (Fig. S34 and Table S15).[20] Given the accuracy of the predicted spectroscopic parameters, all orbital analysis presented in the main text utilized the wavefunctions computed using this method.

For the calculation of XAS spectra, the TPSSh functional was used in conjunction with the def2-TZVP basis set on all non-Fe atoms and the CP(PPP) basis set for Fe. The angular integration grid was set to Grid4 (NoFinalGrid), with increased radial accuracy for the Fe atom (IntAcc 7). To simulate solid state effects, a continuum solvation model was included (COSMO) with an infinite dielectric. TD-DFT transitions were calculated using the Tamm-Dancoff approximation with excitations restricted from the Fe 1*s* orbital. The first 50 lowest-energy transitions were calculated, and the total intensity was computed including both dipole and quadrupole transition intensities. To calibrate the energy scale of the computed spectra, the XAS spectrum of ($PhBP_3^{iPr}$)Fe≡N was calculated from BP86-ZORA optimized coordinates, and compared with the experimentally-reported spectrum.[21] A constant shift of 154.25 eV was determined to align the intense pre-edge transitions of the experimental and calculated spectra; subsequently, this same shift was applied to all calculated spectra. A line broadening of 1.5 eV was applied to the calculated spectra to approximate the experimentally-observed linewidth. Spectra were normalized by setting the area of the ($PhBP_3^{iPr}$)Fe≡N spectrum to 0.92, which is the estimated area normalized to the edge-jump (based on the related

($PhBP_3^{CH2Cy}$)Fe≡N variant).[21] To compare with the experimental pre-edge spectra, the line-broadened TD-DFT spectrum was fit to 2 or 3 Gaussian functions, from which predicted pre-edge areas were calculated.

**Supplementary Discussion**

Excited state paramagnetism of ($P_3^B$)Fe($NNMe_2$)

The chemical shifts of the NMR resonances of complex ($P_3^B$)Fe($NNMe_2$) were found to be strongly temperature dependent, with significant deviations from linearity when plotted versus $T^{-1}$. This observation is consistent with the thermal occupation of a paramagnetic excited state, as has been observed for the isoelectronic hydrazido complex [($P_3^{Si}$)Fe($NNMe_2$)]$^+$.[22] This temperature dependence can be modelled accurately as a low-spin/high-spin equilibrium by adopting a simple model assuming: (i) rapid interconversion of the spin states on the NMR timescale; (ii) temperature independence of the diamagnetic shift; (iii) Curie-behavior for the paramagnetic shift; and (iv) a Boltzmann distribution of states. Under these assumptions, the observed chemical shift will be the Boltzmann-weighted sum of those of the diamagnetic state and the paramagnetic state,

$$\begin{aligned}\delta_{obs} &= \delta_d \cdot \gamma_d + \delta_p \cdot \gamma_p \\ &= \delta_d \cdot (1-\gamma_p) + \left(\delta_d + \frac{C}{T}\right) \cdot \gamma_p \\ &= \delta_d + \frac{C}{T} \cdot \gamma_p \\ &= \delta_d + \frac{C}{T} \cdot \frac{g_p}{g_p + \exp\left(\frac{1}{R}\left(\frac{\Delta H}{T} - \Delta S\right)\right)} \end{aligned} \quad (1)$$

Where $\delta_d$ is the diamagnetic shift, $C$ is the Curie factor of the paramagnetic shift, and $g_p$ is the electronic degeneracy of the excited state. Fitting this equation to both the temperature dependence of the *N*-$CH_3$ resonance from $^1$H NMR (which has the largest Curie factor) and the $^{31}$P chemical shift produces $\Delta H$ = 3.7(1) kcal mol$^{-1}$ and $\Delta S$ = 2(3) cal mol$^{-1}$ K$^{-1}$ for $g_p$ = 3 and $\Delta H$ = 3.7(1) and $\Delta S$ = 0(2) for $g_p$ = 5 (Fig. S35 and Table S12). The fits are of equivalent quality, therefore, while $\Delta H$ is well-determined from the variable temperature NMR data, $g_p$ is not. However, on the basis of computational studies (*vide infra*, Table S14), we assign $g_p$ = 3 (i.e. a triplet excited state), given that a quintet state is predicted to be > 20 kcal mol$^{-1}$ higher in energy than the diamagnetic ground state.

XRD refinement details for ($P_3^B$)Fe($NNMe_2$)

The crystal structure of ($P_3^B$)Fe($NNMe_2$) suffered from two-part positional disorder of the two *N*-methyl carbons (CM1, CM2), coupled with two-part positional disorder of the isopropyl substituents on P2. This disorder reflects rotation about the N1—N2 bond by ca. 30°, which forces the isopropyl substituents on P2 to rotate away from CM2 to avoid unfavorable steric clashing. Each position of the two-part disorder was located in the difference map and refined anisotropically with hydrogen atoms calculated in the usual manner. To test the robustness of this model, the occupancies of both

conformations of the $NNMe_2$ ligand and both conformations of the P2 substituents were refined separately. The major conformations refined to 64% and 65% occupancy, respectively, confirming that the two conformational changes are coupled.

Mössbauer simulation details

All spectra were fit assuming symmetric quadrupole doublets with Lorentzian line shapes. This is the correct model for frozen solution spectra in the limit of fast electronic relaxation, which is typical at 80 K. However, the presence of small amounts of multiple (possibly paramagnetic and not necessarily in the fast relaxation limit) contaminants prevents accurate integration of spectra collected from protonation experiments of $[(P_3^B)FeN_2]^{2-}$ and $[Na(12\text{-crown-}4)_2][(P_3^B)Fe(N_2)]$ at long mixing times. However, given the well-separated spectral features of nitrido $[(P_3^B)Fe{\equiv}N]^+$, masking the spectra from $\delta = -2.2$ to 2.8 mm $s^{-1}$ allowed for accurate integrations of $[(P_3^B)Fe{\equiv}N]^+$, when present. The results of simulations including the minimal number of quadrupole doublets necessary for a reasonable simulation ($\chi^2$ near 1) are given in Tables S2–S5, where the integrations of $[(P_3^B)Fe{\equiv}N]^+$ from masking the interior region of the spectra are also given. The latter integrations should be taken as more accurate.

EXAFS simulation details

The EXAFS spectrum of $(P_3^B)Fe(NNMe_2)$ was initially refined using phase and amplitude functions from the McHale curved wave theory tables included in EXAFSPAK, finding a prominent peak in the phase-uncorrected Fourier transform at $R + \Delta \sim 1.9$ Å due to three P-atom scatterers and a smaller peak at $R + \Delta \sim 1.5$ Å due to a single N-atom scatterer. Using coordinates from XRD, a model was constructed including the intact $NNMe_2$ ligand as well as a single *i*$Pr_2$P moiety bonded to the B atom through a phenylene linker (i.e. all "symmetry-inequivalent" atoms of the pseudo-$C_3$ symmetric molecule). This model was used as input for the calculation of *ab initio* phase and amplitude functions using FEFF. In addition to single-scattering paths for the $N_\alpha$ atom of the $NNMe_2$ ligand and the P atom, two single-scattering paths due to carbon atoms were found to contribute significantly to the spectrum. One involves the C atom of the phenylene linker bonded directly to B (Fe–C = 3.38 Å from XRD), while the other involves a methyne C atom on the P *i*Pr substitutent (Fe–C = 3.42 Å from XRD). Finally, a single multiple-scattering path was found involving the nearly linear Fe–N–N vector (Fe–N–N = 2.97 Å and < FeNN = 176° from XRD); inclusion of this multiple-scattering path was necessary to completely simulate the Fourier-transformed EXAFS in the region from 0–3 Å. Inclusion of a path due to a B atom scatter improves the simulation marginally; however, with $Z = 5$, the B atom only weakly scatters the Fe photoelectron, which is reflected in the relatively high uncertainty in the simulated parameters. If the multiple-scattering path is omitted from the simulation, the data in the region $R + \Delta > 2$ Å is poorly fit (Fig. S36).

For simulation of the EXAFS spectra of $(P_3^B)Fe(NNH_2)$ and $[(P_3^B)Fe{\equiv}N]^+$, the phase and amplitude functions computed from the XRD coordinates of $(P_3^B)Fe(NNMe_2)$ were employed. As expected, the EXAFS spectrum of $(P_3^B)Fe(NNH_2)$ was found be very similar to that found for $(P_3^B)Fe(NNMe_2)$. A single N-atom scatterer and 3 P-atom scatterers account for the majority of the spectrum below $R + \Delta = 2.5$ Å. Inclusion of two C-atom scatterers and the Fe–N–N multiple scattering path found above for

$(P_3^B)Fe(NNMe_2)$ was necessary to model the data above $R + \Delta = 2.5$ Å. The latter is consistent with a still-intact N–N bond in $(P_3^B)Fe(NNH_2)$. Inclusion of a B atom scatterer improves the simulation only marginally, and the fitted parameters for this path obtains a somewhat higher degree of uncertainty compared with the other shells. As before, if the multiple-scattering path is omitted from the simulation, the data in the region $R + \Delta > 2$ Å is poorly fit (Fig. S36).

The EXAFS spectrum of $[(P_3^B)Fe{\equiv}N]^+$ is dominated by a single N-atom scatterer and 3 P-atom scatterers below $R + \Delta = 2.5$ Å. Beyond this, two prominent peaks in the Fourier transformed data at $R + \Delta = 2.8$ and 3.2 Å were simulated as ligand C atom scatterers. The slightly longer Fe–C distances found in $[(P_3^B)Fe{\equiv}N]^+$ are consistent with the observed elongation of the Fe–P bonds, which is also reproduced in the DFT calculated structure. (N.B., based on the DFT structure, we can assign the short C-atom scatterer as the phenylene C bonded P rather than that bonded to B, Fe–C = 3.40 Å.) To determine whether the phase and amplitude functions calculated from the crystal structure of $(P_3^B)Fe(NNMe_2)$ lead to any error in the measured bond lengths of $[(P_3^B)Fe{\equiv}N]^+$, we re-calculated single-scattering phase and amplitude functions using the refined N and P distances of $[(P_3^B)Fe{\equiv}N]^+$. However, using these new phase and amplitude functions did not alter the fitted Fe–N or Fe–P distances. Notably, no peak appears at ca. 2.5 Å (observed in $(P_3^B)Fe(NNH_2)$ and $(P_3^B)Fe(NNMe_2)$ from the Fe–N–N multiple scatterer), which suggests cleavage of the previously-intact N–N bond. Using the refined Fe–N–N distance of ca. 3 Å from $(P_3^B)Fe(NNH_2)$ and $(P_3^B)Fe(NNMe_2)$, the Fe–N bond length of 1.54(2) Å of $[(P_3^B)Fe{\equiv}N]^+$, $\Delta R = 0.1$ Å for $k_{max} = 16$ Å$^{-1}$, and assuming a quasi-linear Fe–N–N vector, the *absence* of such a peak implies an N–N bond length > 1.5 Å, if it were still present. This is significantly longer than the N–N single bond of $N_2H_4$, and thus the most consistent interpretation of the data is complete rupture of the N–N bond in $[(P_3^B)Fe{\equiv}N]^+$, in accordance with the Mössbauer data.

Comparing the set of second scans with the set of first scans of the sample of $[(P_3^B)Fe{\equiv}N]^+$, there is a noticeable reduction in the intensity of the pre-edge feature at 7112.1 eV (reduced by ~20%; Fig. S37), suggesting photodamage upon exposure to the high-energy X-rays. However, despite the changes in the pre-edge region, simulation of the EXAFS region on the set of second scans reveals no changes in the observed interatomic distances, within error (Table S9). A plausible hypothesis is thus clean photoreduction of the Fe(IV) nitrido to its formally Fe(III) congener.[23] Given the relatively small amount of 3*d* character calculated for the $a_1$-symmetry LUMO of $[(P_3^B)Fe{\equiv}N]^+$, photoreduction would be expected to produce an $S = 1/2$ ground state with significant delocalization of the radical onto the N and B atoms. As a result, a resonance structure involving Fe(IV) and a ligand-centered radical would be a strong contributor, and little change in the Fe-ligand bond distances is expected. A comparison of the DFT-calculated structures of $[(P_3^B)Fe{\equiv}N]^+$ ($S = 0$) and $(P_3^B)Fe{\equiv}N$ ($S = 1/2$) corroborates this prediction, revealing changes in the Fe–N and Fe–P interatomic distances that would not be resolved by EXAFS (<< 0.1 Å; Table S17).

To test the robustness of the deglitching procedure used on the raw data, the EXAFS spectra of $(P_3^B)Fe(NNH_2)$ and $[(P_3^B)Fe{\equiv}N]^+$ were additionally simulated in the range $k = 2$–$12$ Å$^{-1}$, using the unaltered raw data. Within experimental error, the fitted parameters were identical to the simulations of the deglitched data, although inclusion of a B-atom scatterer and the second C-atom scatterer in the simulation of $(P_3^B)Fe(NNH_2)$

resulted in negative $\sigma^2$, and were thus excluded. We also note that although Fe impurities were present in the samples of $(P_3^B)Fe(NNH_2)$ and $[(P_3^B)Fe{\equiv}N]^+$ examined by XAS (> 70% and 60% pure, respectively, Fig. S25), attempts to include additional scattering shells (e.g. P or N/O atoms) from these impurities did not significantly improve the simulations. This is mostly like due to the fact that, in both cases, no single impurity is present in more than ~20% yield. However, the presence of impurities may be the cause of the moderately large $\sigma^2$ values for the Fe–N scatterers in $(P_3^B)Fe(NNH_2)$ and $[(P_3^B)Fe{\equiv}N]^+$. For example, if $N$ for the N-atom scatterer of $[(P_3^B)Fe{\equiv}N]^+$ is allowed to refine freely, the best-fit value changes from $N = 1$ to $N = 0.77$, which is accompanied by a 0.002 $Å^2$ reduction in $\sigma^2$. Setting $N = 0.7$ and including a second N-atom scatterer at 1.66 Å results in a very minor improvement to the simulation (< 1% in $\chi^2$). Moreover, this has no effect on the best-fit value for the nitrido N-atom distance $R$ (1.53(2) Å), within error. Given typical uncertainties of 20% in $N$, these were restricted to 1 for both N-atom scatterers of $(P_3^B)Fe(NNH_2)$ and $[(P_3^B)Fe{\equiv}N]^+$, for simplicity.

The EXAFS spectrum of $[(P_3^B)FeN_2]^{2-}$ was simulated in the same fashion as that of $(P_3^B)Fe(NNMe_2)$, except *ab initio* phase and amplitude functions were computed from the DFT-optimized coordinates of $[(P_3^B)FeN_2]^{2-}$. Again, in addition to N and P scatterers, two shells of ligand C-atom scatterers and a single Fe–N–N multiple-scatterer were included to simulate the EXAFS spectrum above $R + \Delta = 2.5$ Å. In this case, the degeneracy of one C scatterer was increased from 3 to 6 to include the phenylene C bonded to the P atom (Fe—C = 3.34 Å from DFT). Attempts to include a B atom scatterer resulted in unreasonably large uncertainties in $\sigma^2$, presumably due to the greater number and intensity of Fe—C paths, and this path was thus excluded.

*N.B.* For those simulations where inclusion of a Fe–N–N multiple scattering path was found to be necessary to fully simulate the data, an estimate of the N–N interatomic distance can be obtained by subtraction of the distance of the Fe–N single scattering path from that of the multiple scattering path.

NMR Spectra

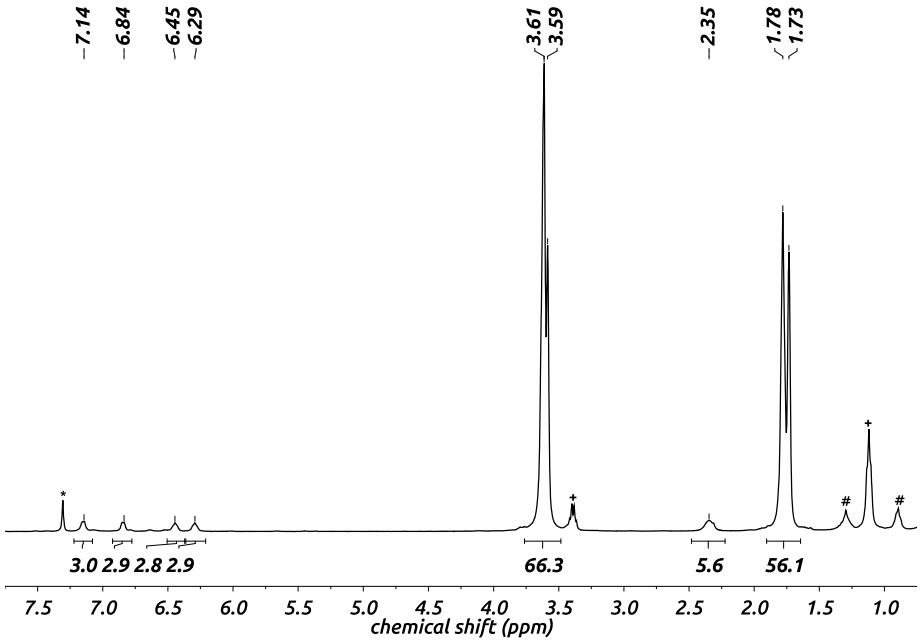


**Fig. S1.**

$^{1}$H NMR spectrum of $[(P_3^B)FeN_2]^{2-}$ (400 MHz, $d_8$-THF, 293 K) produced from *in situ* reduction of $[Na(12\text{-crown-}4)_2][(P_3^B)Fe(N_2)]$. Owing to the slight shift of the residual THF resonances due to interaction with Lewis acidic $K^+$ ions, the chemical shifts were referenced internally to a $C_6H_6$ standard at 7.31 ppm (denoted by *). Accurate integrations for the isopropyl methyl protons of the ligand and the methylene protons of the $[(12\text{-crown-}4)_2Na]^+$ ion could not be obtained due to overlap with the residual THF resonances appearing at 1.73 and 3.59 ppm. $^+$Denotes $Et_2O$ impurity. $^\#$Denotes *n*-pentane impurity.

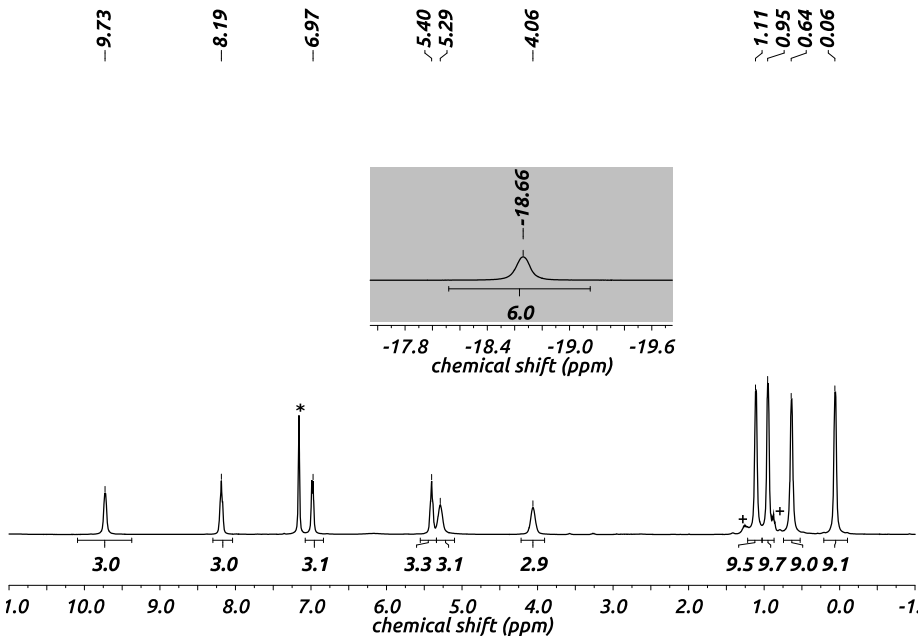


**Fig. S2.**

$^{1}$H NMR spectrum of ($P_3^B$)Fe(NNMe$_2$) (400 MHz, $C_6D_6$, 293 K). Inset shows the resonance due to the *N*-methyl protons. *Denotes residual $C_6H_6$ signal. $^{+}$Denotes trace *n*-pentane impurity.

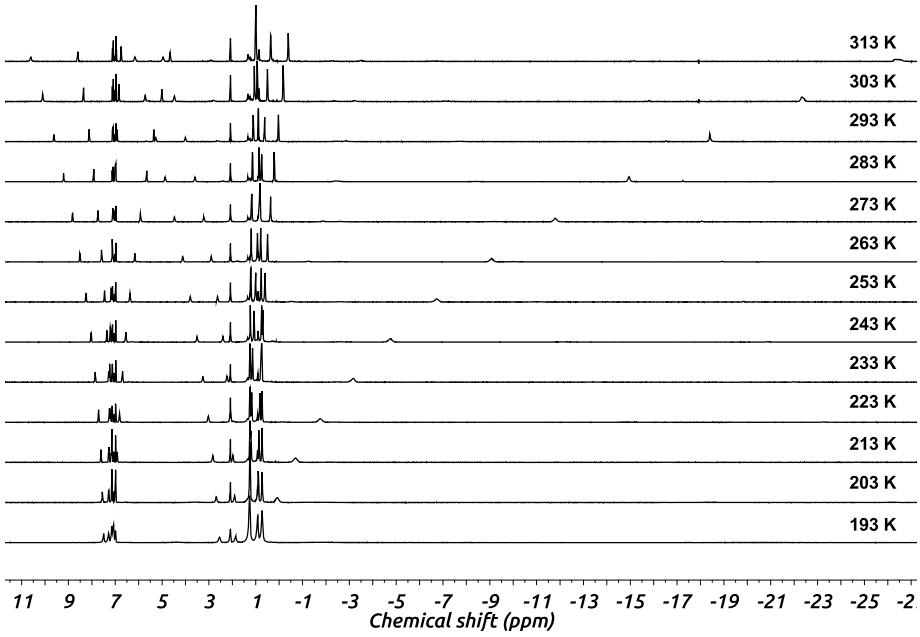


**Fig. S3.**

Variable temperature $^{1}$H NMR spectra of ($P_3^B$)Fe(NNMe$_2$) (500 MHz, $d_8$-toluene). Temperatures of individual spectra are indicated on the right. The large magnitude of the Curie factor of the *N*-CH$_3$ resonance is evident by its highly temperature dependent position, relative to the $P_3^B$ ligand-based proton signals.

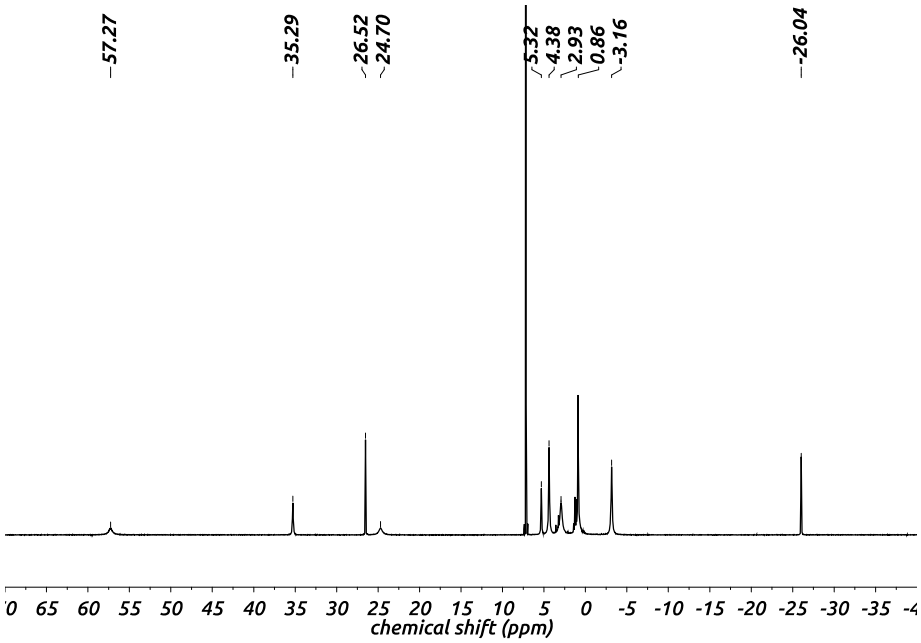


**Fig. S4.**
$^{1}$H NMR spectrum of ($P_3^B$)Fe(OTf) (400 MHz, $C_6D_6$, 293 K).

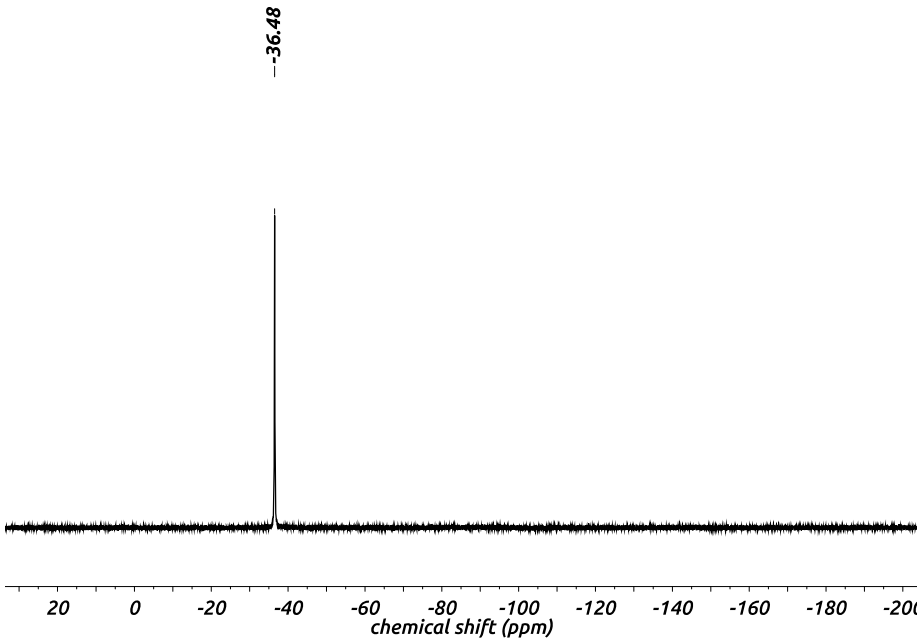


**Fig. S5.**
$^{19}$F NMR spectrum of ($P_3^B$)Fe(OTf) (376 MHz, $C_6D_6$, 293 K).

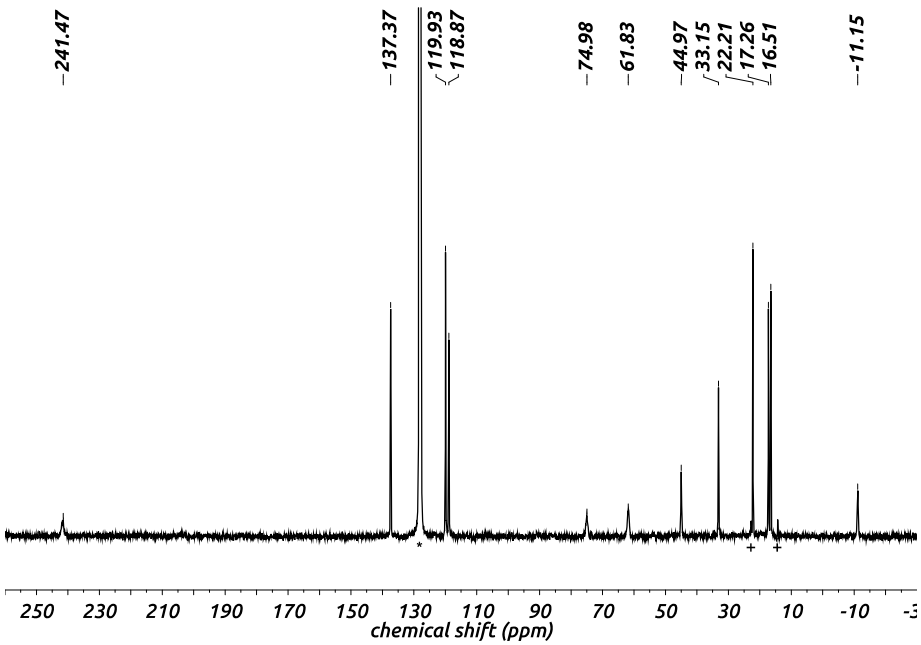


**Fig. S6.**

$^{13}$C NMR spectrum of ($P_3^B$)Fe(NNMe$_2$) (101 MHz, $C_6D_6$, 293 K). *Denotes residual $C_6H_6$ signal. $^+$Denotes trace *n*-pentane impurity. Note that a resonance for the *N*-methyl carbon could not be observed at this temperature, even over a range of 1000 to −500 ppm.

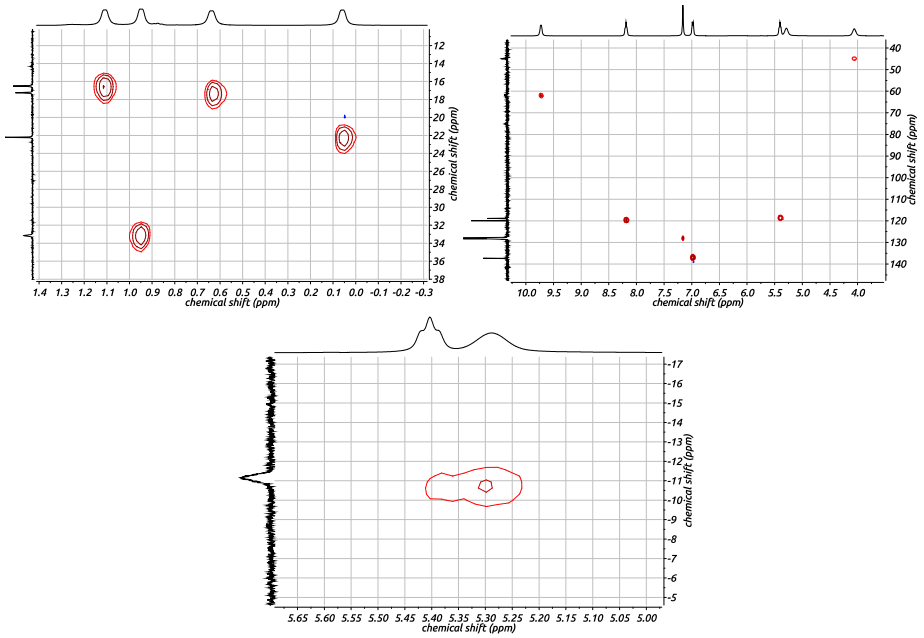


**Fig. S7.**
$^{1}H$–$^{13}C$ HMQC spectra of ($P_3^B$)Fe($NNMe_2$) ($^{1}H$ 400 MHz, $^{13}C$ 101 MHz, $C_6D_6$, 293 K). Abscissa: $^{1}H$ chemical shifts; Ordinate: $^{13}C$ chemical shifts.

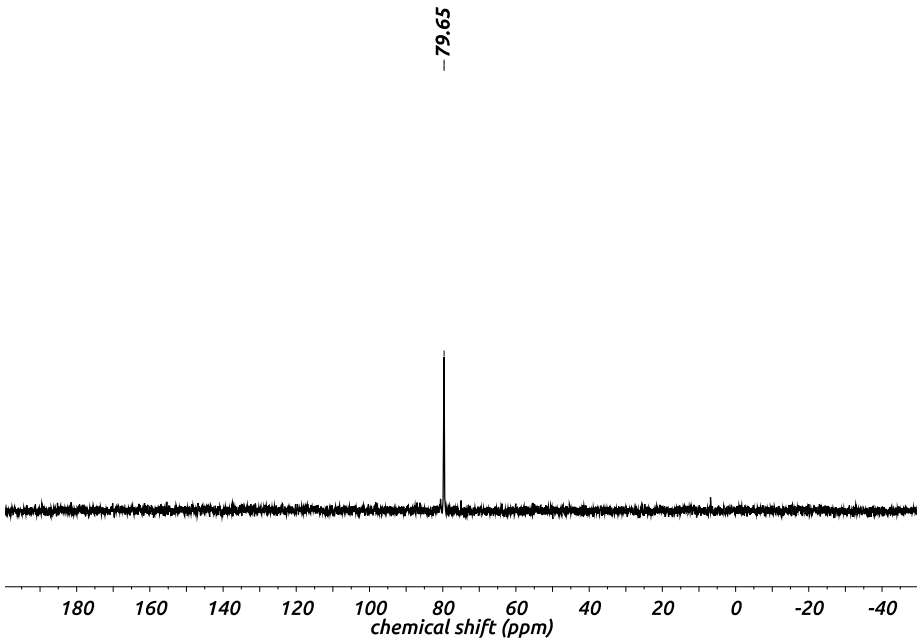


**Fig. S8.**

$^{31}$P NMR spectrum of $[(P_3^B)FeN_2]^{2-}$ (162 MHz, $d_8$-THF, 293 K) produced from *in situ* reduction of $[Na(12\text{-crown-}4)_2][(P_3^B)Fe(N_2)]$.

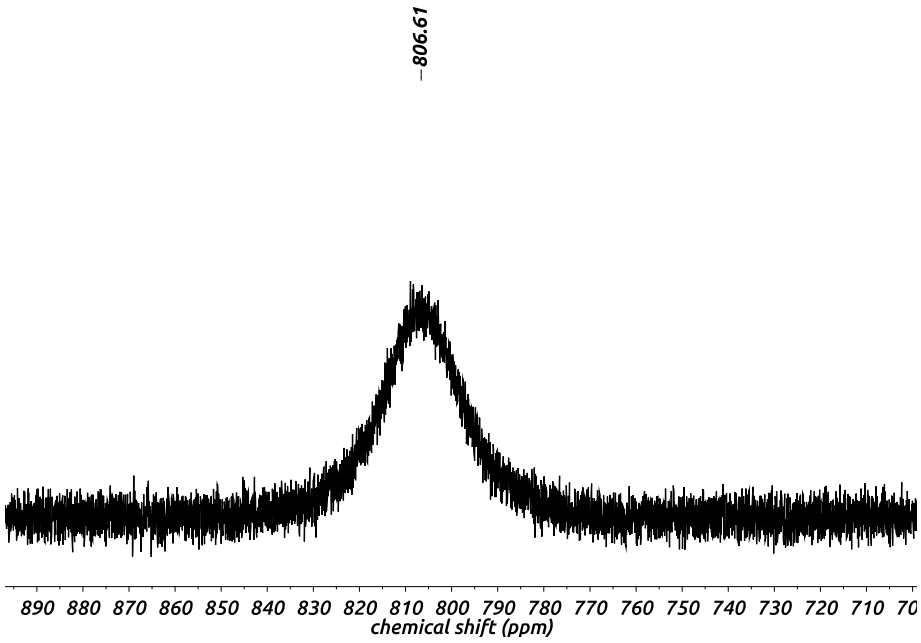


**Fig. S9.**
$^{31}$P NMR spectrum of ($P_3^B$)Fe(NNMe$_2$) (162 MHz, $C_6D_6$, 293 K).

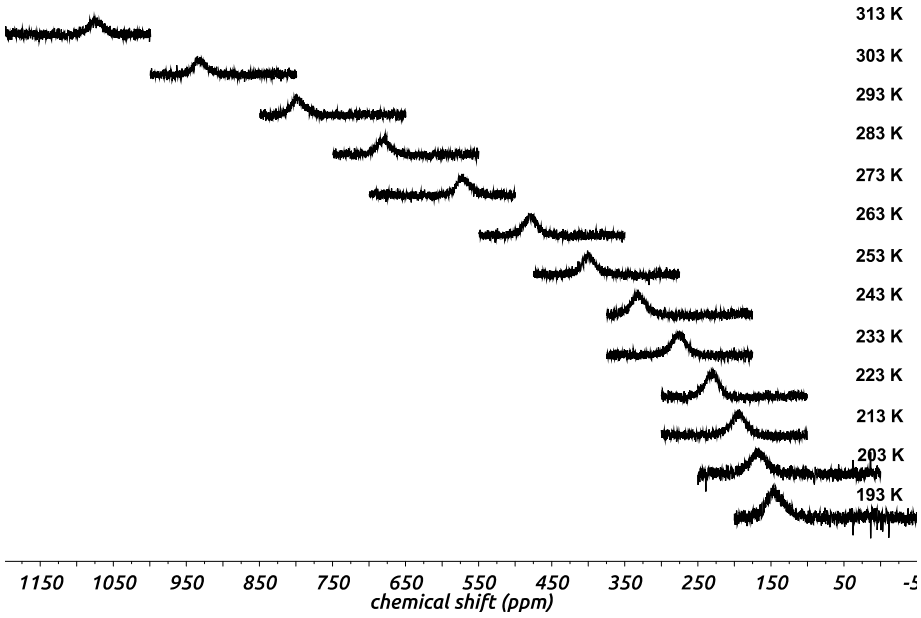


**Fig. S10.**

Variable temperature $^{31}$P NMR spectra of ($P_3^B$)Fe(NNMe$_2$) (202 MHz, $d_8$-toluene). Temperatures of individual spectra are indicated on the right.

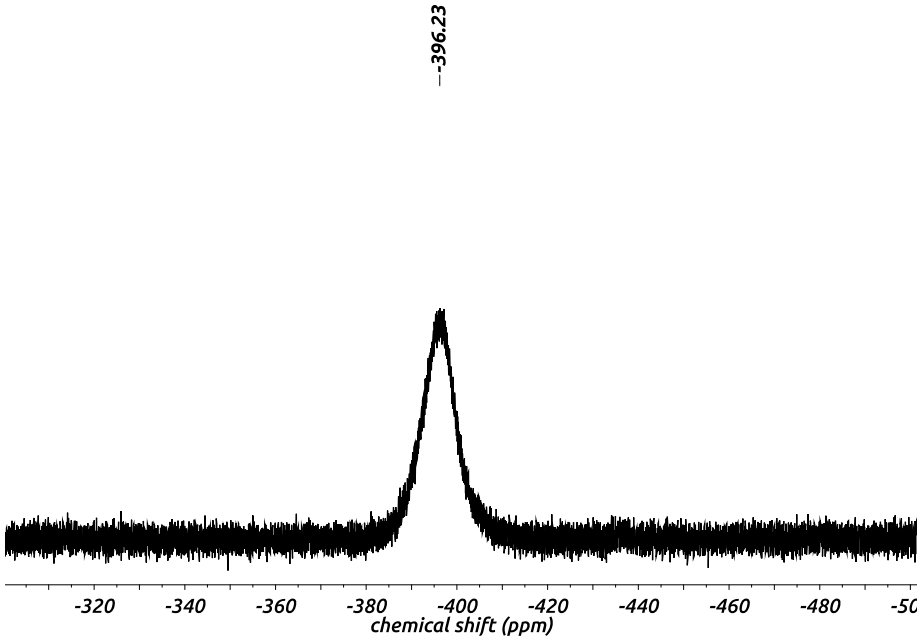


**Fig. S11.**
$^{11}$B NMR spectrum of ($P_3^B$)Fe(NNMe$_2$) (128 MHz, $C_6D_6$, 293 K).

IR Spectra

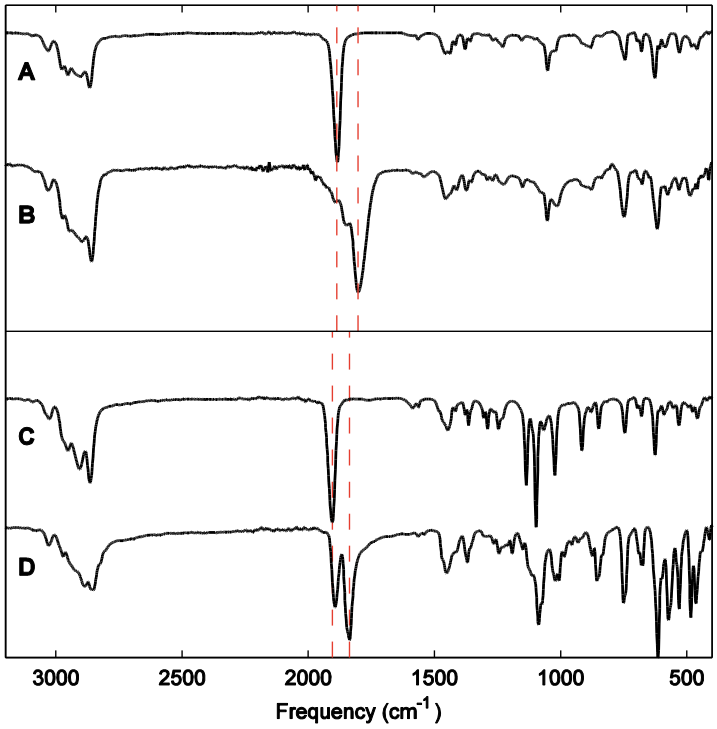


**Fig. S12.**

(**A**) IR spectrum of $[Na(Et_2O)_2][(P_3^B)Fe(N_2)]$ deposited as a thin film from a THF solution. (**B**) IR spectrum of $[(P_3^B)FeN_2]^{2-}$ generated *in situ* from a THF solution of $[Na(Et_2O)_2][(P_3^B)Fe(N_2)]$ by iterative passage through a column of $KC_8$, and depositing as a thin film. (**C**) IR spectrum of $[Na(12\text{-crown-4})_2][(P_3^B)Fe(N_2)]$ deposited as a thin film from a THF solution. (**D**) IR spectrum of $[(P_3^B)FeN_2]^{2-}$ generated from a DME solution of $[Na(12\text{-crown-4})_2][(P_3^B)Fe(N_2)]$ by iterative passage through a column of $KC_8$, and subsequent recrystallization. The spectrum was collected on a powder generated from the recrystallized material and shows contamination with $[K(DME)_x][(P_3^B)FeN_2]$ ($\nu_{NN}$ = 1893 $cm^{-1}$). The red dashed lines in the top panel are at energies 1886 and 1803 $cm^{-1}$ while the red dashed lines in the bottom panel are at energies 1904 and 1836 $cm^{-1}$.

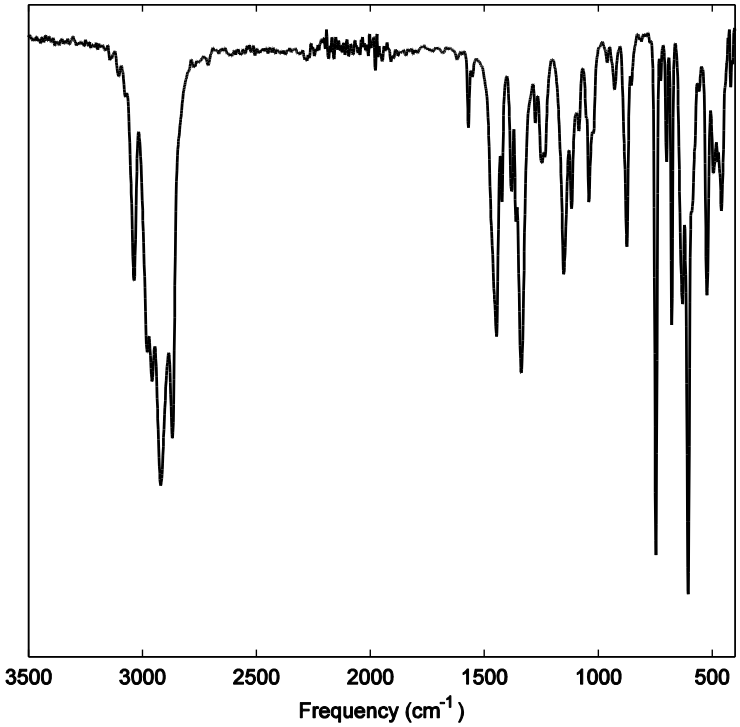


**Fig. S13.**
IR spectrum of $(P_3^B)Fe(NNMe_2)$ deposited as a thin film from a $C_6D_6$ solution.

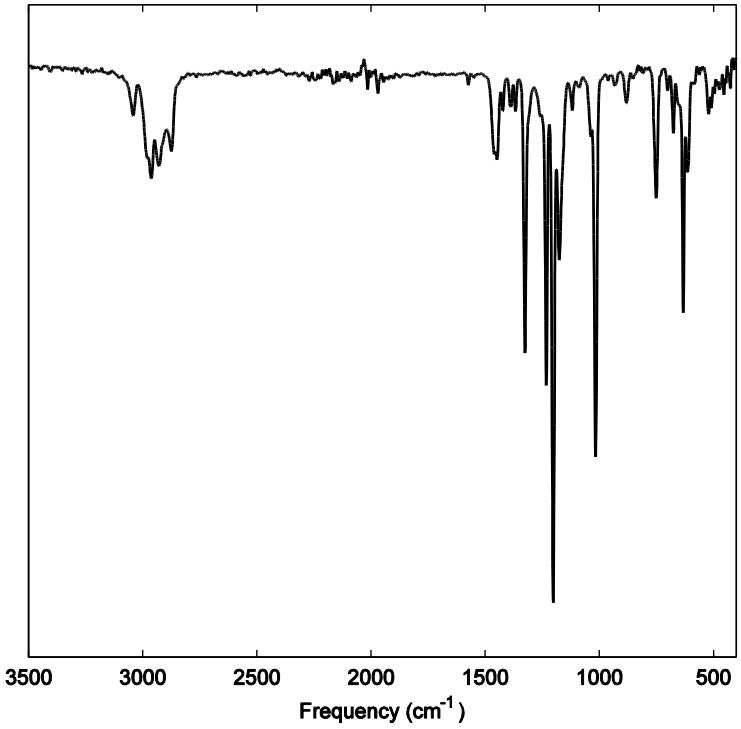


**Fig. S14.**
IR spectrum of ($P_3^B$)Fe(OTf) deposited as a thin film from a $C_6D_6$ solution.

UV-vis Spectra

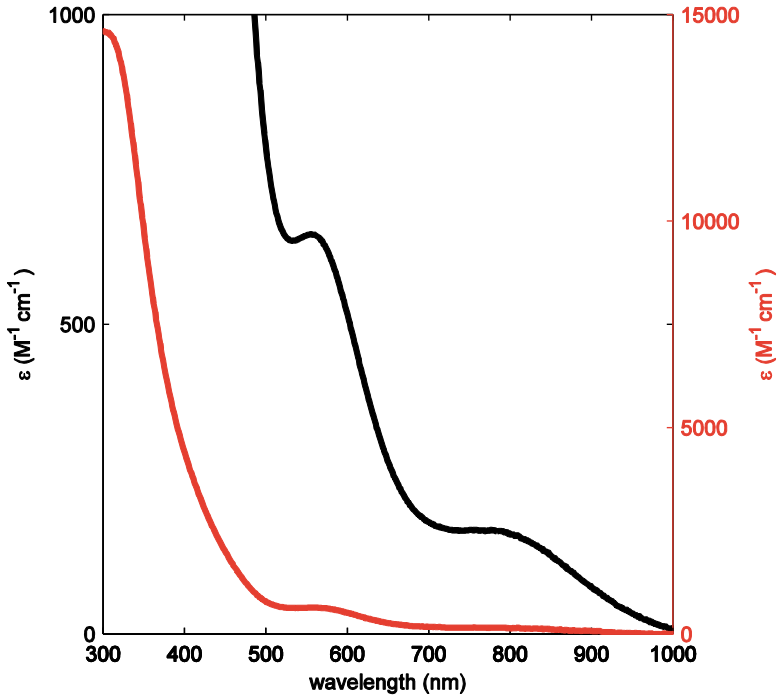


**Fig. S15.**

UV-visible spectrum of $(P_3^B)Fe(NNMe_2)$ (toluene, 293 K). The black trace corresponds to the left axis scale, while the red trace corresponds to the right axis scale.

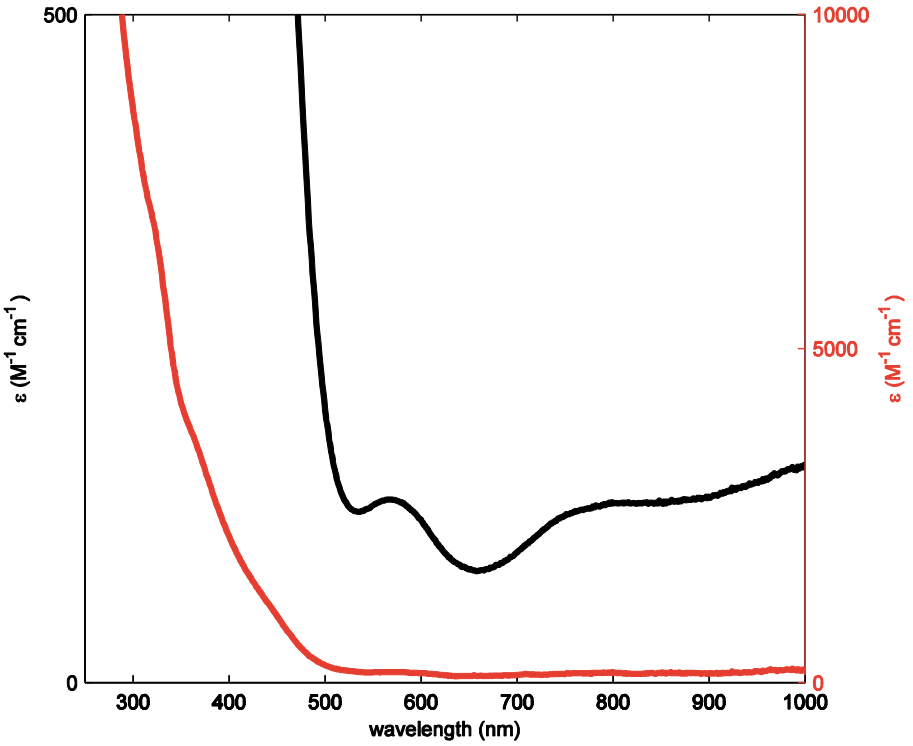


**Fig. S16.**

UV-visible spectrum of ($P_3^B$)Fe(OTf) (2-MeTHF, 293 K). The black trace corresponds to the left axis scale, while the red trace corresponds to the right axis scale.

Mössbauer Spectra

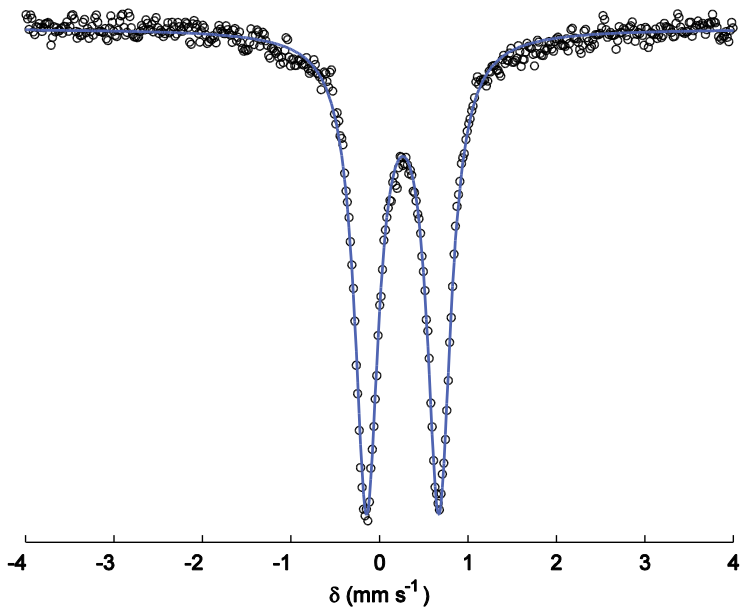


**Fig. S17.**

Mössbauer spectrum of $[(P_3^B)FeN_2]^{2-}$ generated from *in situ* reduction of $^{57}$Fe labelled $[Na(12\text{-crown-}4)_2][(P_3^B)Fe(N_2)]$ in THF (1.4 mM; sample was frozen as a suspension with excess $KC_8$). The spectrum was collected at 80 K in the presence of a 50 mT magnetic field oriented parallel to the γ-ray propagation. Raw data are shown as open circles, simulation as a solid line. Simulation parameters: $\delta = 0.26$ mm s$^{-1}$; $|\Delta E_Q| = 0.82$ mm s$^{-1}$; $\Gamma = 0.32$ mm s$^{-1}$.

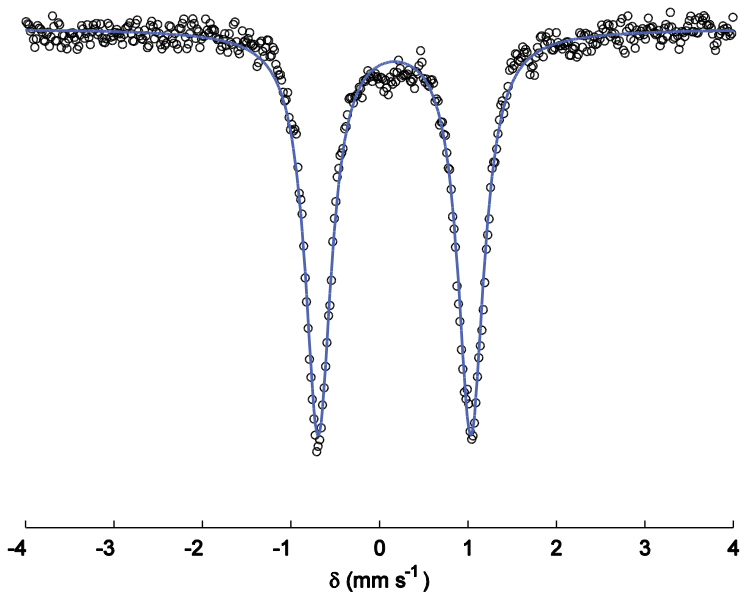


**Fig. S18.**

Mössbauer spectrum of $(P_3^B)Fe(NNMe_2)$ as a frozen solution in 2-MeTHF (30 mM; natural abundance $^{57}Fe$). The spectrum was collected at 80 K in the presence of a 50 mT magnetic field oriented parallel to the γ-ray propagation. Raw data are shown as open circles, simulation as a solid line. Simulation parameters: $\delta = 0.17$ mm $s^{-1}$; $|\Delta E_Q| = 1.73$ mm $s^{-1}$; $\Gamma = 0.36$ mm $s^{-1}$.

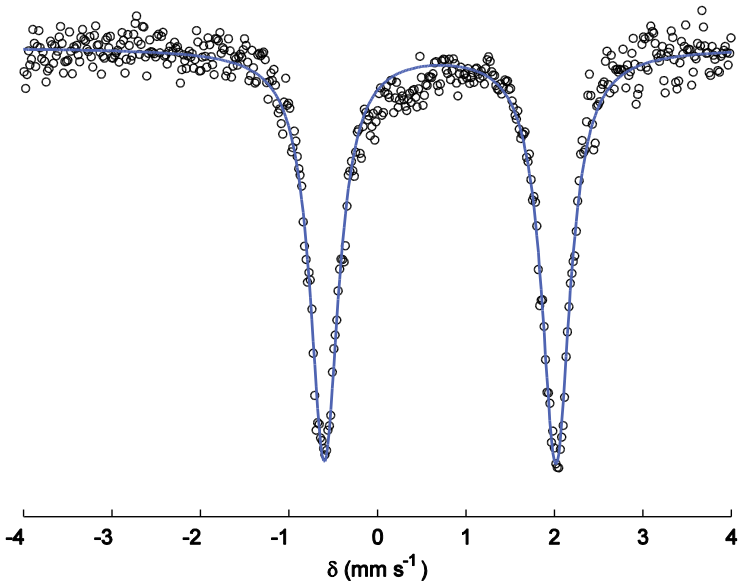


**Fig. S19.**

Mössbauer spectrum of $(P_3^B)Fe(OTf)$ as a powder suspended in boron nitride (natural abundance $^{57}Fe$). The spectrum was collected at 80 K in the presence of a 50 mT magnetic field oriented parallel to the γ-ray propagation. Raw data are shown as open circles, simulation as a solid line. Simulation parameters: $\delta = 0.71$ mm $s^{-1}$; $|\Delta E_Q| = 2.62$ mm $s^{-1}$; $\Gamma = 0.39$ mm $s^{-1}$.

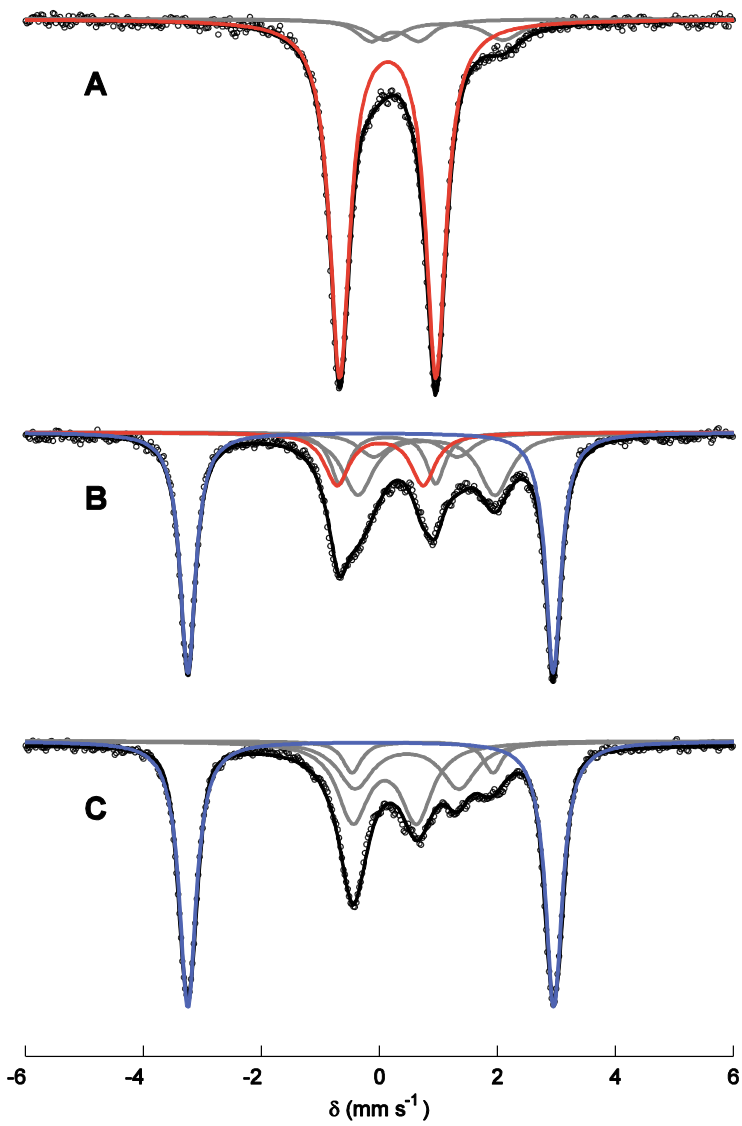


**Fig. S20.**

Freeze-quenched Mössbauer spectra from protonation studies of $^{57}$Fe labelled $[(P_3^B)FeN_2]^{2-}$ using TfOH as the proton source. Spectra were collected as frozen 2-MeTHF solutions at 80 K in the presence of a 50 mT magnetic field oriented parallel to the γ-ray propagation. Raw data are shown as open circles, simulation as a solid black line, with individual sub-spectra plotted in grey, red, and blue. Full simulation parameters are given in Table S2. (**A**) Reaction freeze-quenched after 15 min. of mechanical mixing, showing the major species to be $(P_3^B)Fe(NNH_2)$ (red sub-spectrum). (**B**) Reaction freeze-quenched after 60 min. of mechanical mixing, showing ca. 50% yield of $[(P_3^B)Fe{\equiv}N]^+$ (blue sub-spectrum) and ca. 10% yield of $(P_3^B)Fe(NNH_2)$ (red sub-spectrum). (C) Reaction freeze-quenched after 120 min. of mechanical mixing, showing ca. 60% yield of $[(P_3^B)Fe{\equiv}N]^+$ (blue sub-spectrum), and complete consumption of $(P_3^B)Fe(NNH_2)$.

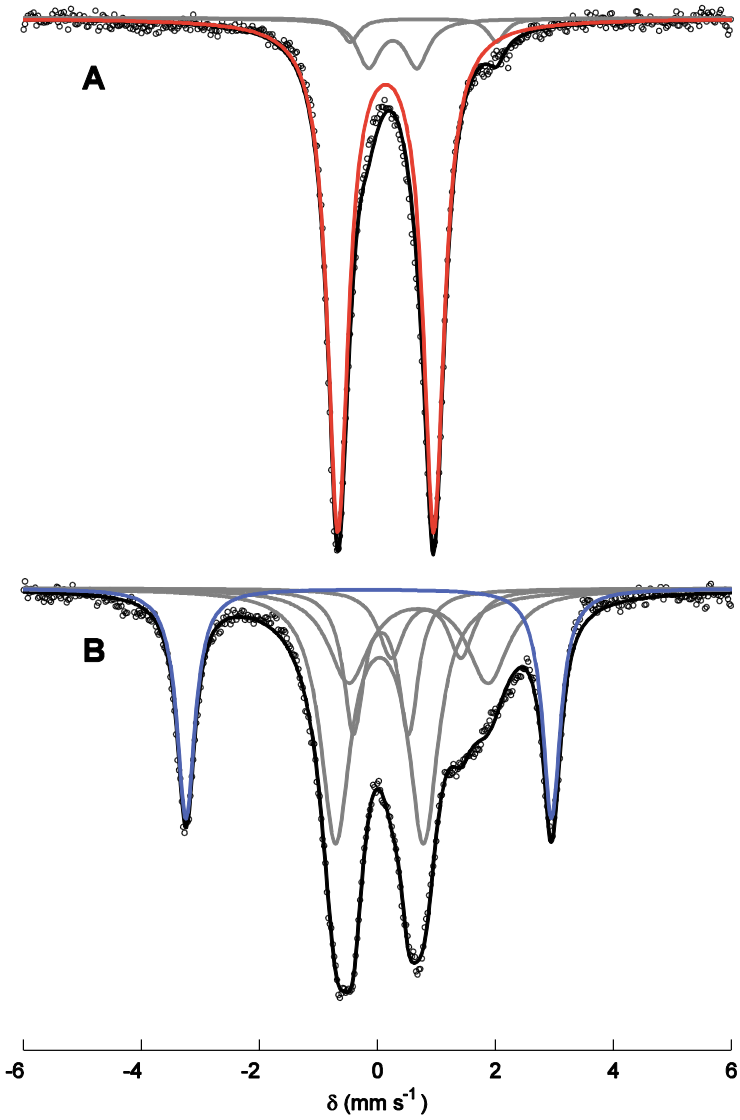


**Fig. S21.**

Freeze-quenched Mössbauer spectra from protonation studies of $^{57}$Fe labelled $[(P_3^B)FeN_2]^{2-}$ using $HBAr^F_4$ as the proton source. Spectra were collected as frozen 2-MeTHF solutions at 80 K in the presence of a 50 mT magnetic field oriented parallel to the γ-ray propagation. Raw data are shown as open circles, simulation as a solid black line, with individual sub-spectra plotted in grey, red, and blue. Full simulation parameters are given in Table S3. (**A**) Reaction freeze-quenched after 15 min. of mechanical mixing, showing the major species to be $(P_3^B)Fe(NNH_2)$ (red sub-spectrum). (**B**) Reaction freeze-quenched after 30 min. of mechanical mixing, showing ca. 20% yield of $[(P_3^B)Fe{\equiv}N]^+$ (blue sub-spectrum).

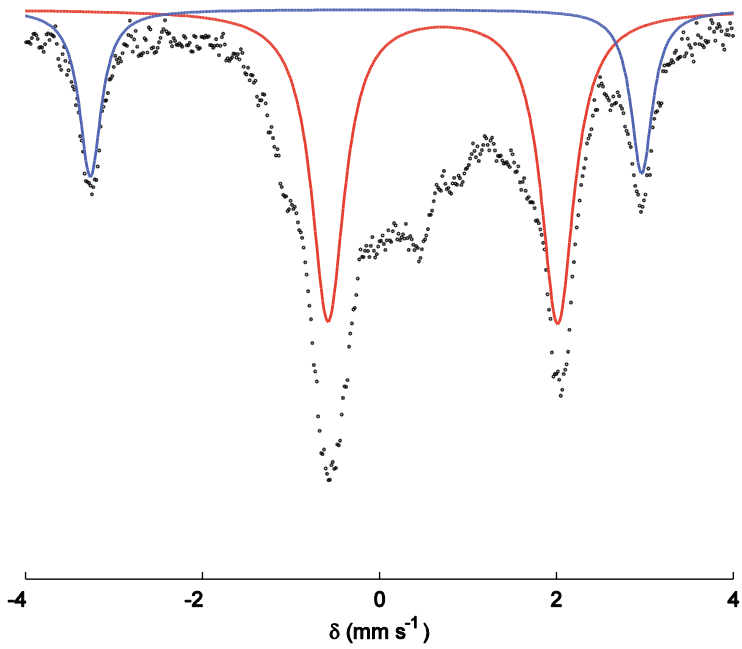


**Fig. S22.**

Freeze-quenched Mössbauer spectra from protonation of $^{57}$Fe labelled [Na(12-crown-4)$_2$][($P_3^B$)Fe($N_2$)] using TfOH as the proton source, mixing for 15 min. in supercooled 2-MeTHF. The spectrum was collected as frozen 2-MeTHF solutions at 80 K in the presence of a 50 mT magnetic field oriented parallel to the γ-ray propagation. Raw data are shown as open circles, with a simulation containing [($P_3^B$)Fe≡N]$^+$ (~20%, blue sub-spectrum) and ($P_3^B$)Fe(OTf) (~50%, red sub-spectrum) shown as solid lines.

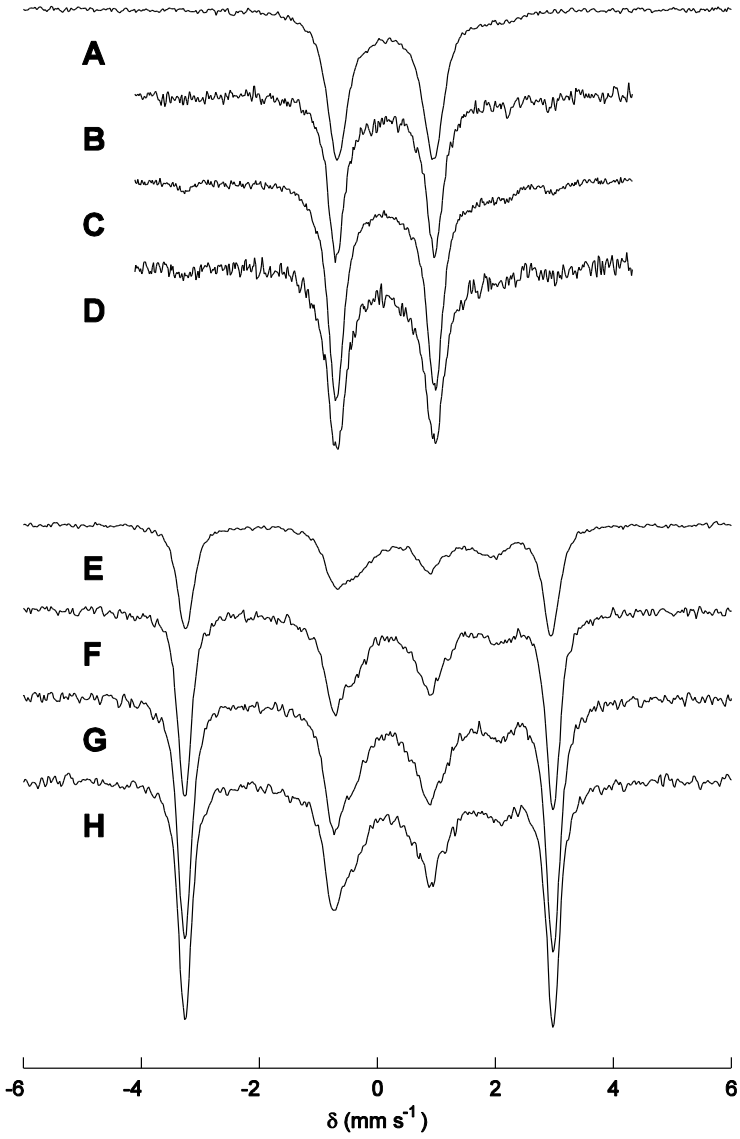


**Fig. S23.**

Freeze-quenched Mössbauer spectra from protonation studies of $^{57}$Fe labelled $[(P_3^B)FeN_2]^{2-}$ using TfOH as the proton source. Spectra **A**–**D** were collected on the sample presented in Figure S20A, while spectra **E**–**H** were collected on the sample presented in Figure S20B. (**A**) Collected at 80 K with a parallel 50 mT magnetic field. (**B**) Collected at 5 K in zero applied field. (**C**) Collected at 5 K with a parallel 50 mT magnetic field. (**D**) Collected at 5 K with a perpendicular 50 mT magnetic field. (**E**) Collected at 80 K with a parallel 50 mT magnetic field. (**F**) Collected at 5 K in zero applied field. (**G**) Collected at 5 K with a parallel 50 mT magnetic field. (**H**) Collected at 5 K with a perpendicular 50 mT magnetic field.

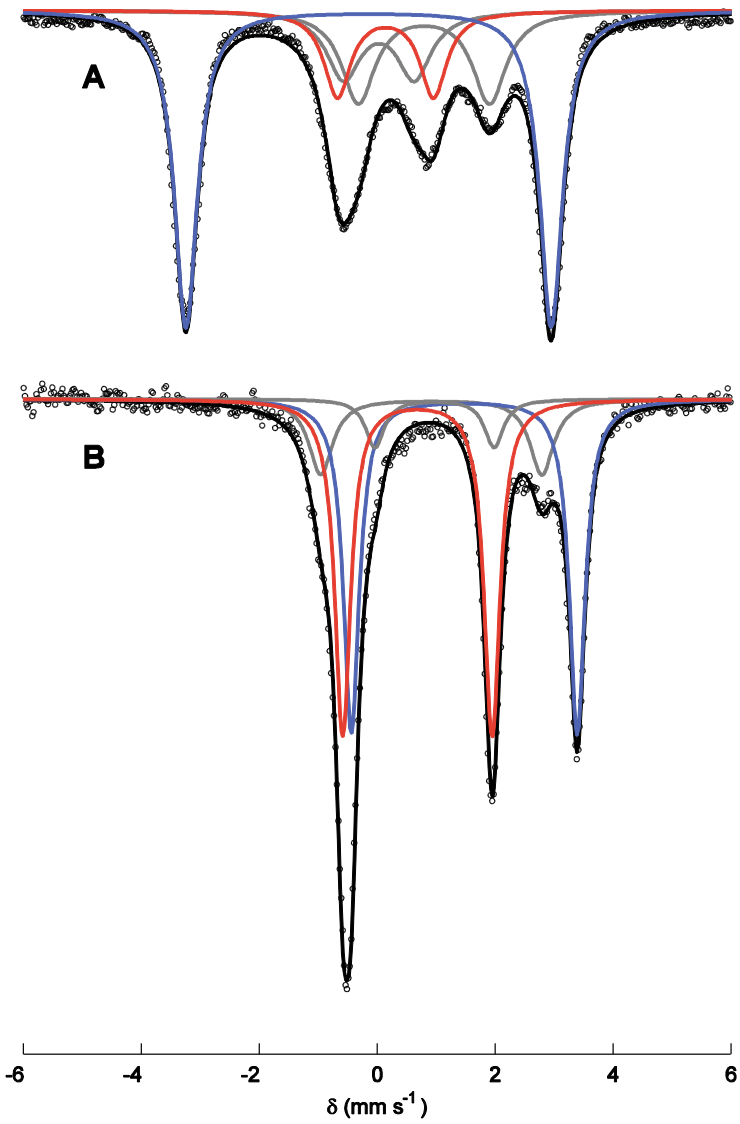


**Fig. S24.**

Freeze-quenched Mössbauer spectra from protonation studies of $^{57}$Fe labelled $[(P_3^B)FeN_2]^{2-}$ using TfOH as the proton source ([Fe] = 4 mM; [TfOH] = 80 mM). Spectra were collected as frozen 2-MeTHF solutions at 80 K in the presence of a 50 mT magnetic field oriented parallel to the γ-ray propagation. Raw data are shown as open circles, simulation as a solid black line, with individual sub-spectra plotted in grey, red, and blue. Full simulation parameters are given in Table S4. (**A**) Reaction freeze-quenched after 30 min. of mechanical mixing, showing ca. 50% yield of $[(P_3^B)Fe{\equiv}N]^+$ (blue sub-spectrum) and ca. 18% yield of $(P_3^B)Fe(NNH_2)$ (red sub-spectrum). (**B**) Spectrum resulting from annealing the sample to room temperature for 10 min, showing decomposition of $(P_3^B)Fe(NNH_2)$ and $[(P_3^B)Fe{\equiv}N]^+$ to a mixture of primarily composed of $(P_3^B)Fe(OTf)$ (42%, red sub-spectrum) and a high-spin Fe(II) species (42%, blue sub-spectrum). A qualitatively similar spectrum is obtained if an identically-prepared sample is annealed to 195 K for longer than 30 minutes.

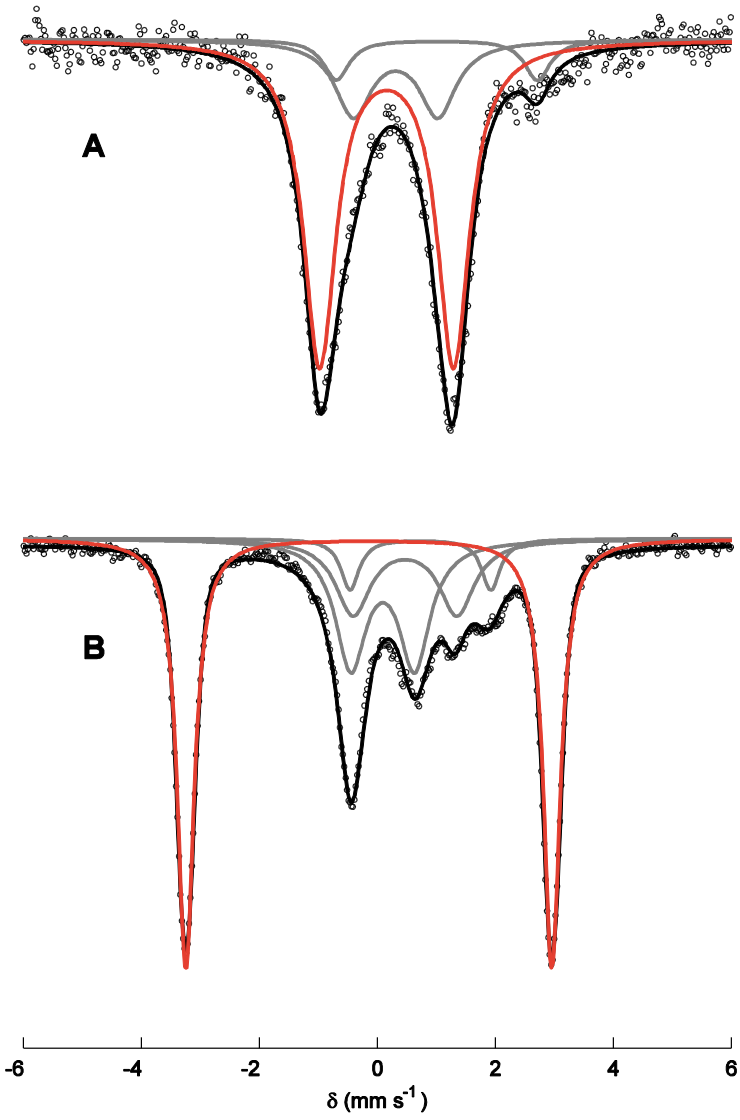


**Fig. S25.**

Freeze-quenched Mössbauer spectra from protonation studies of $^{57}$Fe labelled $[(P_3^B)FeN_2]^{2-}$ using TfOH as the proton source, prepared for XAS studies. Spectra were collected as frozen 2-MeTHF solutions at 80 K in the presence of a 50 mT magnetic field oriented parallel to the γ-ray propagation. Raw data are shown as open circles, simulation as a solid black line, with individual sub-spectra plotted in grey, red, and blue. Full simulation parameters are given in Table S5. (**A**) Reaction freeze-quenched after 15 minutes, showing > 70% of $(P_3^B)Fe(NNH_2)$ (red sub-spectrum). (**B**) Reaction freeze-quenched after 30 min. of mechanical mixing, showing ca. 60% yield of $[(P_3^B)Fe{\equiv}N]^+$ (red sub-spectrum).

XAS Spectra

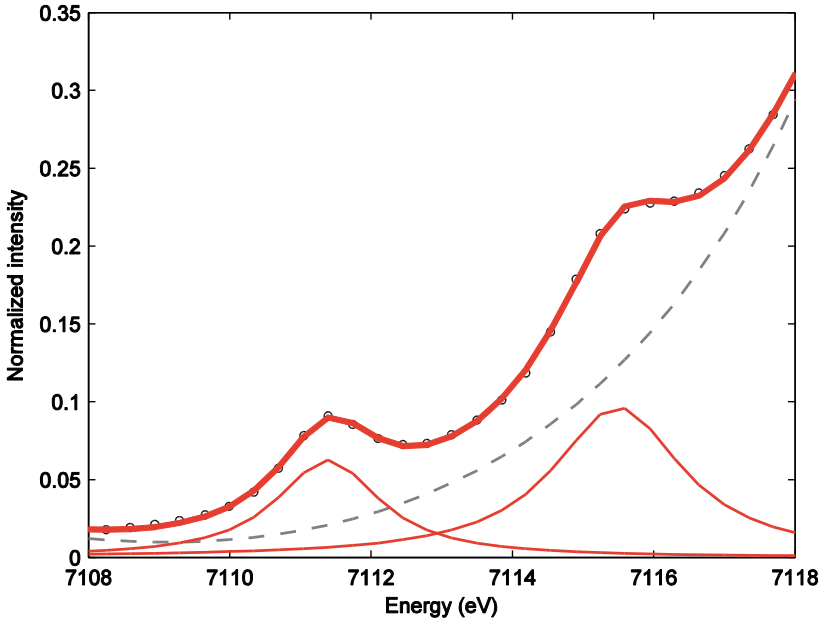


**Fig. S26.**

Pre-edge XANES spectrum of $(P_3^B)Fe(NNMe_2)$. Raw data are shown as open circles, simulation as a bold red line, with individual components as thin red lines and the baseline as a dotted grey line. Full simulation parameters are given in Table S6.

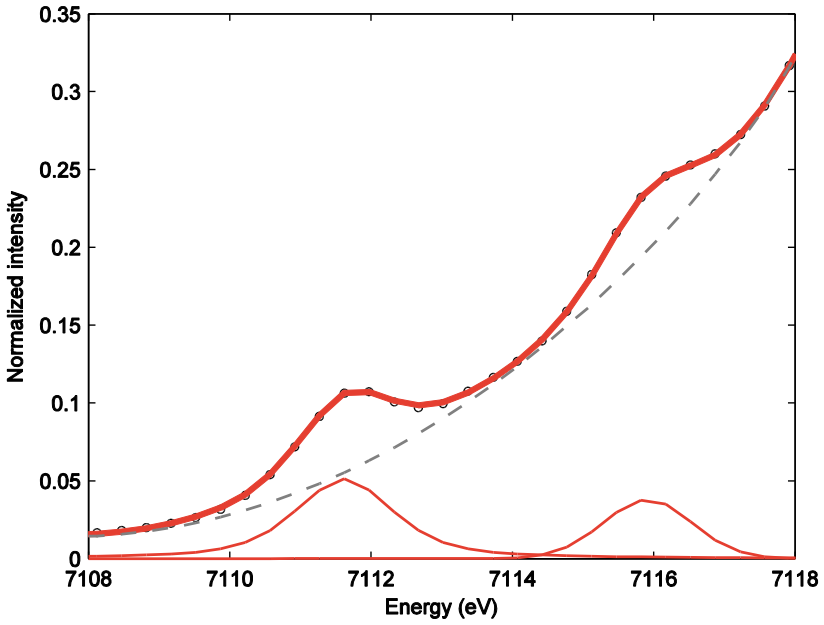


**Fig. S27.**

Pre-edge XANES spectrum of an XAS sample containing predominantly ($P_3^B$)Fe($NNH_2$) (> 70%, see Fig. S25A). Raw data are shown as open circles, simulation as a bold red line, with individual components as thin red lines and the baseline as a dotted grey line. Full simulation parameters are given in Table S6.

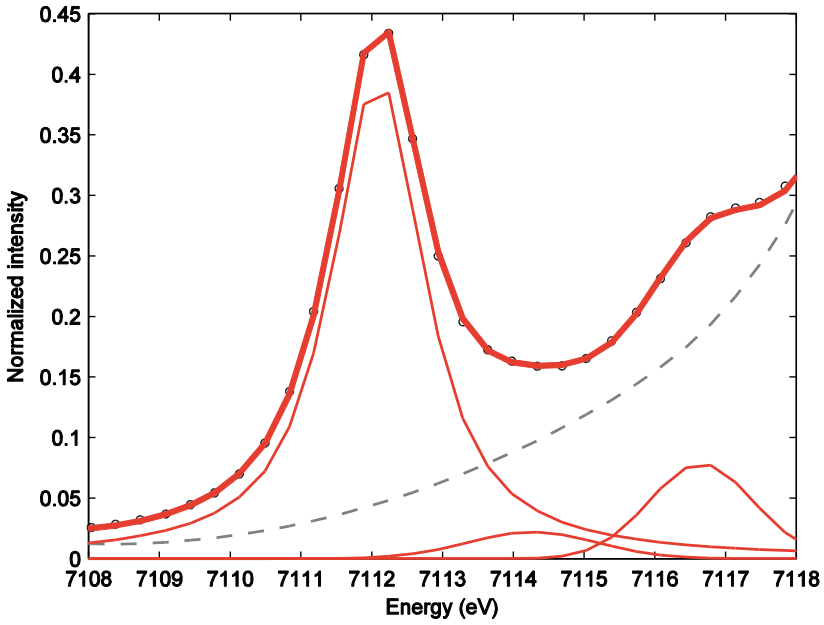


**Fig. S28.**

Pre-edge XANES spectrum of an XAS sample containing predominantly $[(P_3^B)Fe{\equiv}N]^+$ (60%, see Fig. S25B). Raw data are shown as open circles, simulation as a bold red line, with individual components as thin red lines and the baseline as a dotted grey line. Full simulation parameters are given in Table S6.

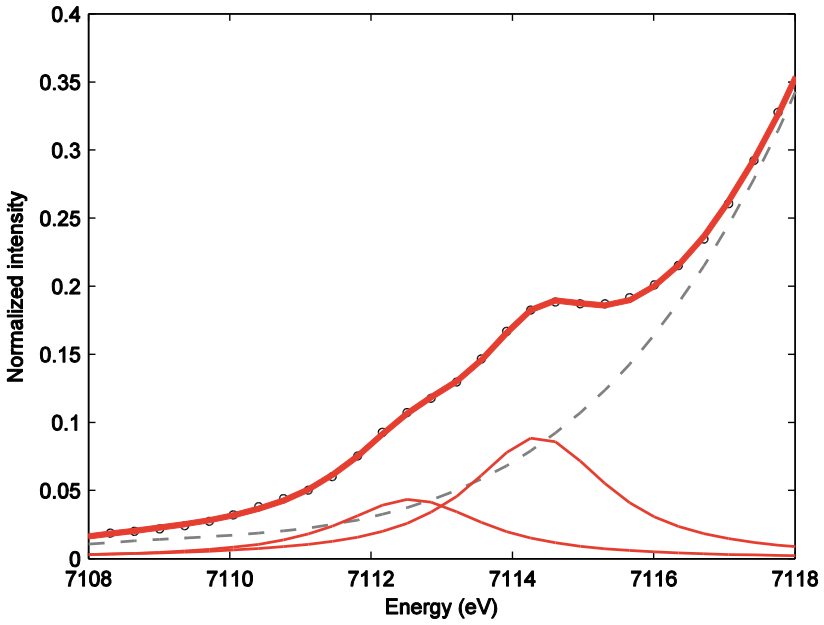


**Fig. S29.**

Pre-edge XANES spectrum of an XAS of $[(P_3{}^B)FeN_2]^{2-}$. Raw data are shown as open circles, simulation as a bold red line, with individual components as thin red lines and the baseline as a dotted grey line. Full simulation parameters are given in Table S6.

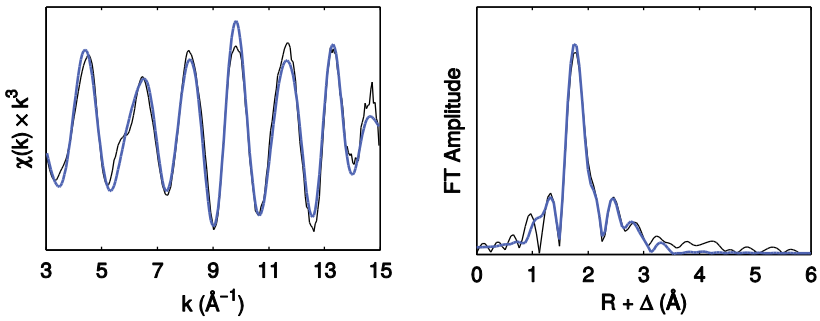


**Fig. S30.**

Raw $k^3$-weighted (left) and Fourier transformed (right) EXAFS data of $[(P_3^B)FeN_2]^{2-}$ prepared *in situ* from the reduction of $[Na(12\text{-crown-}4)_2][(P_3^B)Fe(N_2)]$. The data are presented in black, with the simulation shown in blue. For a complete set of simulation parameters, see table S10.

Cyclic Voltammograms

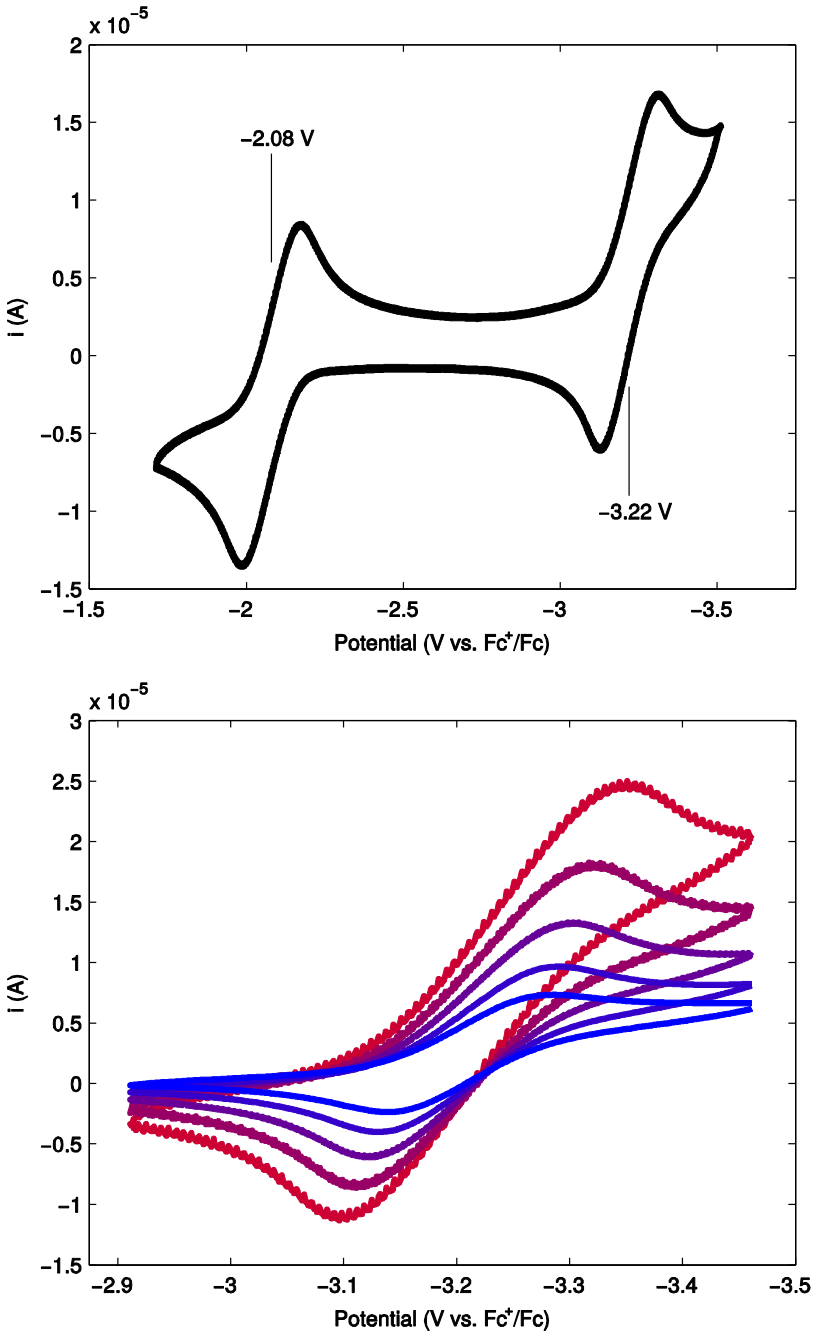


**Fig. S31.**

(Top) Cyclic voltammogram of [Na(12-crown-4)$_2$][($P_3^B$)Fe($N_2$)], scanning in the cathodic direction at a rate of 100 mV $s^{-1}$. (Bottom) Scan rate dependence of the wave observed at −3.2 V in the voltammogram of [Na(12-crown-4)$_2$][($P_3^B$)Fe($N_2$)]. The scan rate was varied by factors of two from 400 (red) to 25 (blue) mV $s^{-1}$.

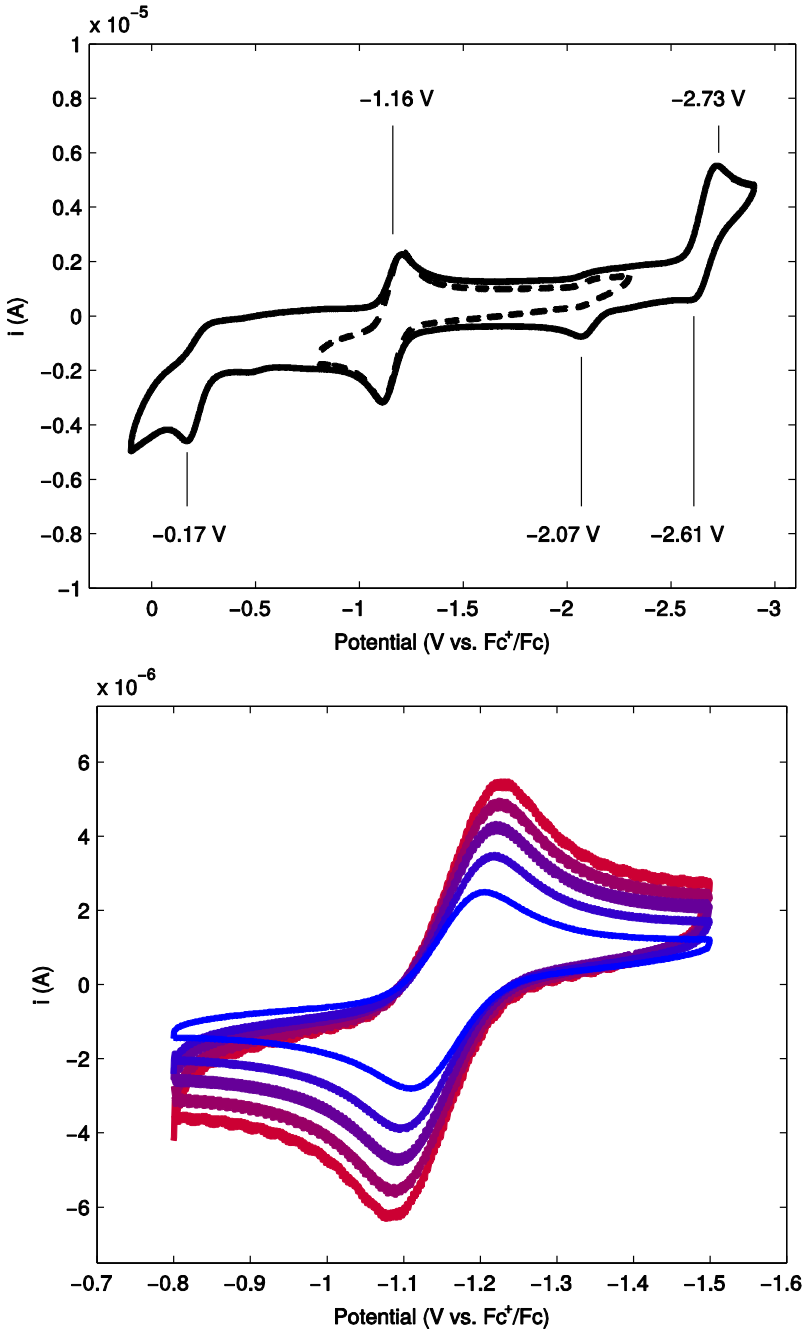


**Fig. S32.**

(Top) Cyclic voltammogram of $(P_3^B)Fe(NNMe_2)$, scanning in the cathodic direction at a rate of 50 mV $s^{-1}$. The dotted lines show a voltammogram scanning from −2.4 to −0.9 V, demonstrating that the feature at −2.07 V appearing in the wider scan results from a decomposition product formed upon one electron reduction. (Bottom) Scan rate dependence of the wave observed at −1.2 V in the voltammogram of $(P_3^B)Fe(NNMe_2)$. The scan rate was varied in increments of 50 mV from 250 (red) to 50 (blue) mV $s^{-1}$.

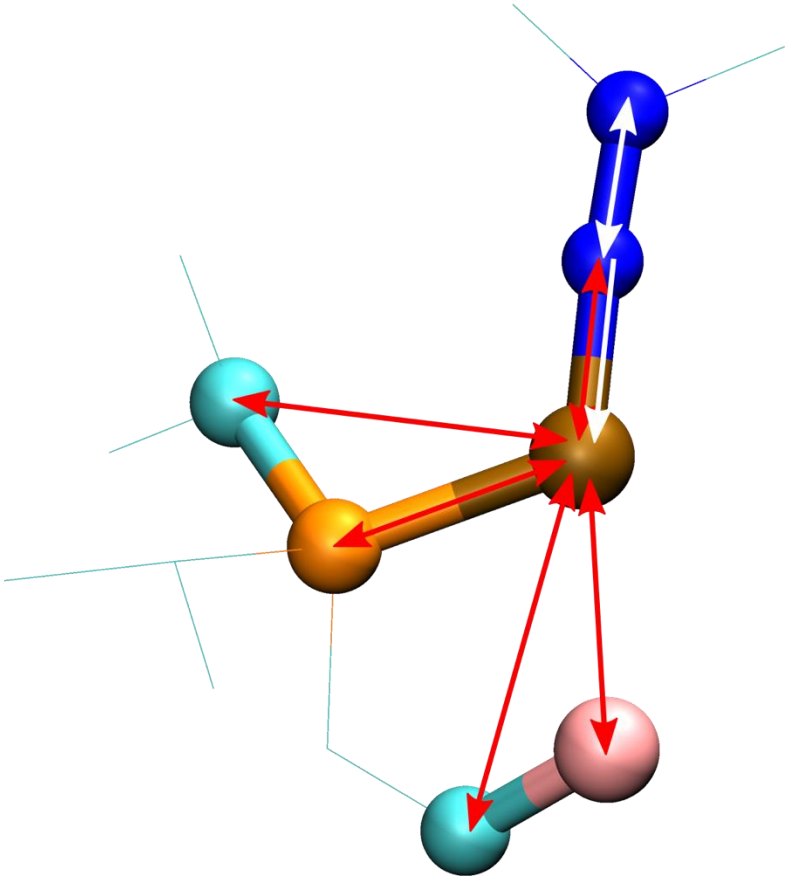

**Fig. S33.**

Single (red arrows) and multiple (white arrows) scattering paths computed by FEFF for ($P_3^B$)Fe(NNMe$_2$) from crystallographic coordinates. Fe is shown in brown, P in orange, N in blue, B in pink, and C in cyan.

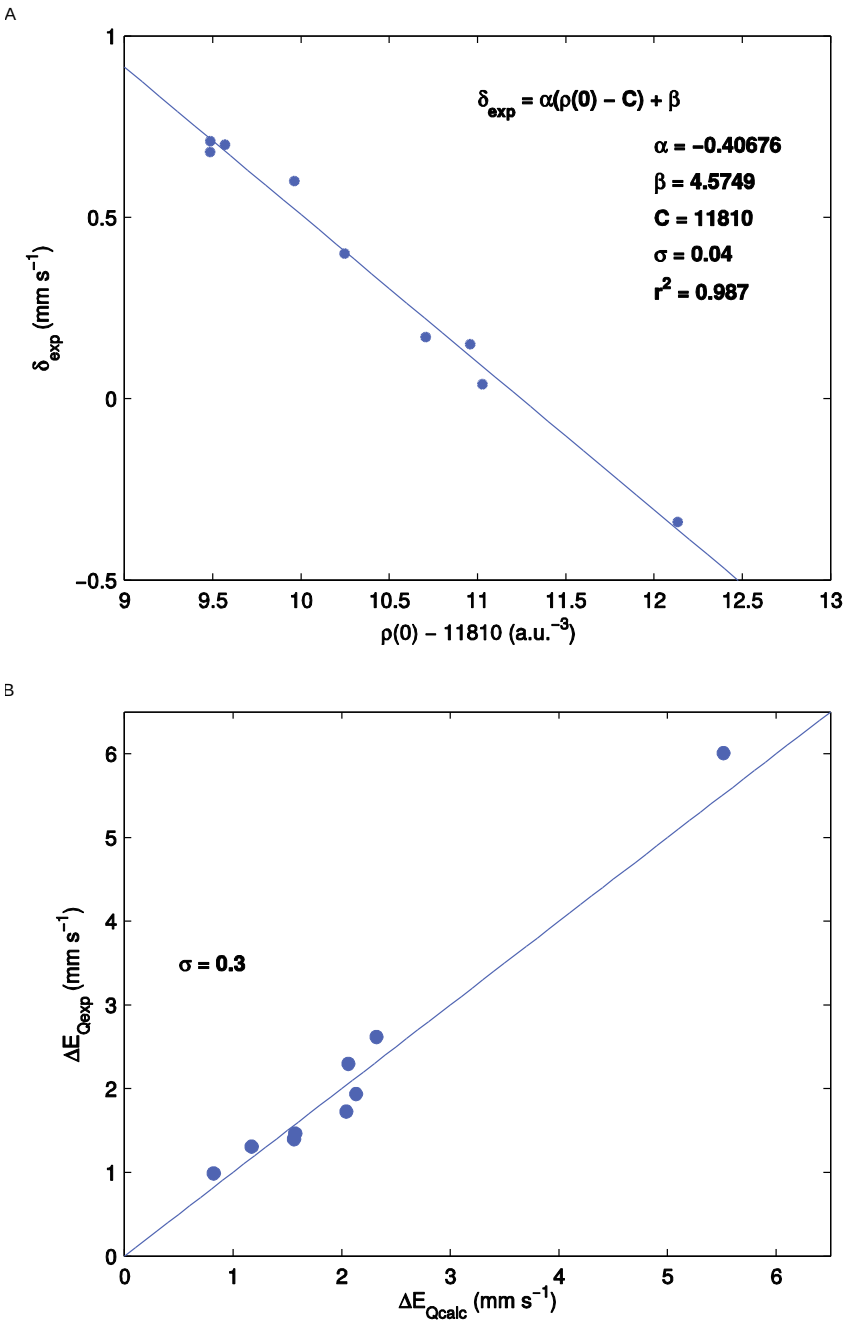


**Fig. S34.**

(**A**) Plot of $\delta_{exp}$ versus ρ(0) – 11810 used to calibrate DFT-predicted isomer shifts. Data (Table S15) are plotted as solid circles, with the least squares linear regression plotted as a solid line. (**B**) Plot of experimental versus calculated quadrupole splittings. Data (Table S15) are plotted as solid circles, with the function $y = x$ plotted as a solid line.

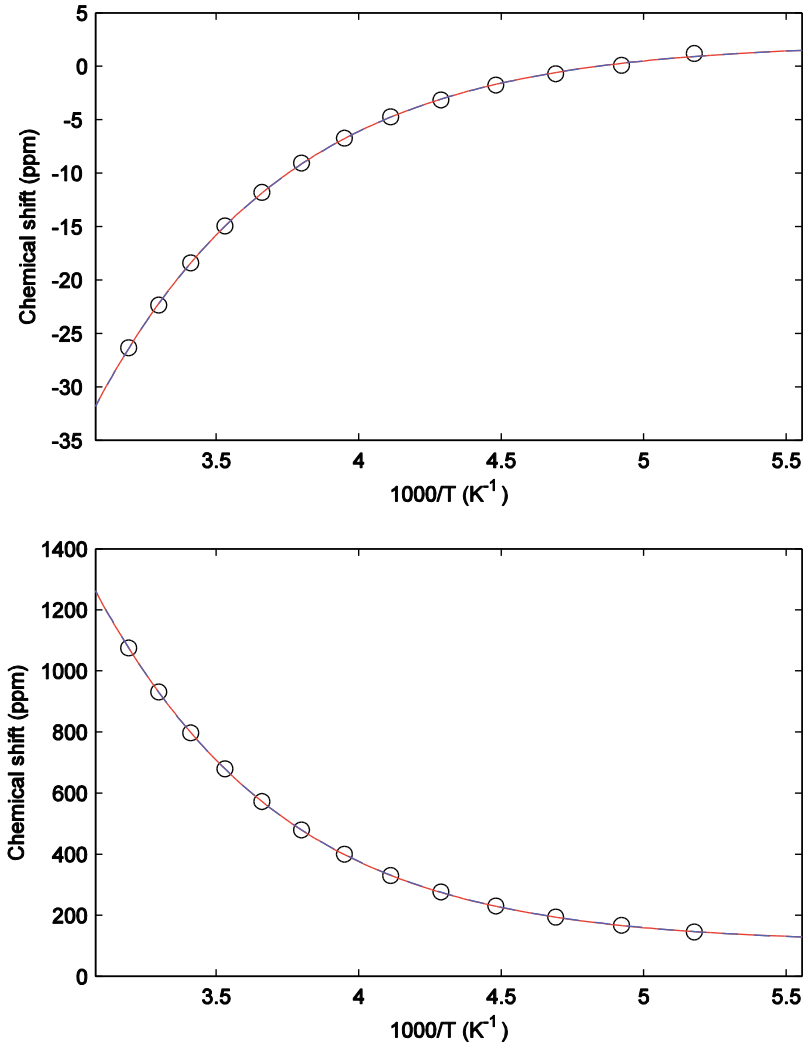


**Fig. S35.**

Plots of chemical shift versus temperature for $(P_3^B)Fe(NNMe_2)$. Data are plotted as open circles, with fits to equation (1) assuming $g_p = 3$ (solid red) and $g_p = 5$ (dashed blue). The top plot shows the behavior of the *N*-$CH_3$ resonance from $^1H$ NMR, while the bottom plot shows the behavior of the $^{31}P$ resonance. The best fit parameters for each curve are given in Table S12.

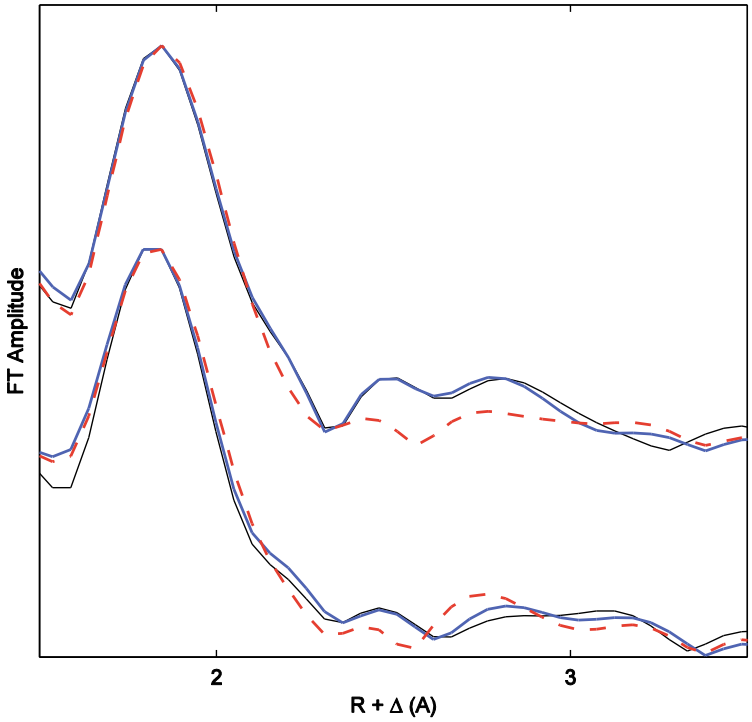


**Fig. S36.**

EXAFS simulations of ($P_3^B$)Fe($NNMe_2$) (top) and ($P_3^B$)Fe($NNH_2$) (bottom) with (solid blue line) and without (dashed red line) inclusion of an Fe–N–N multiple scattering path. See Tables S7 and S8 (simulations 3 and 4) for the simulation parameters.

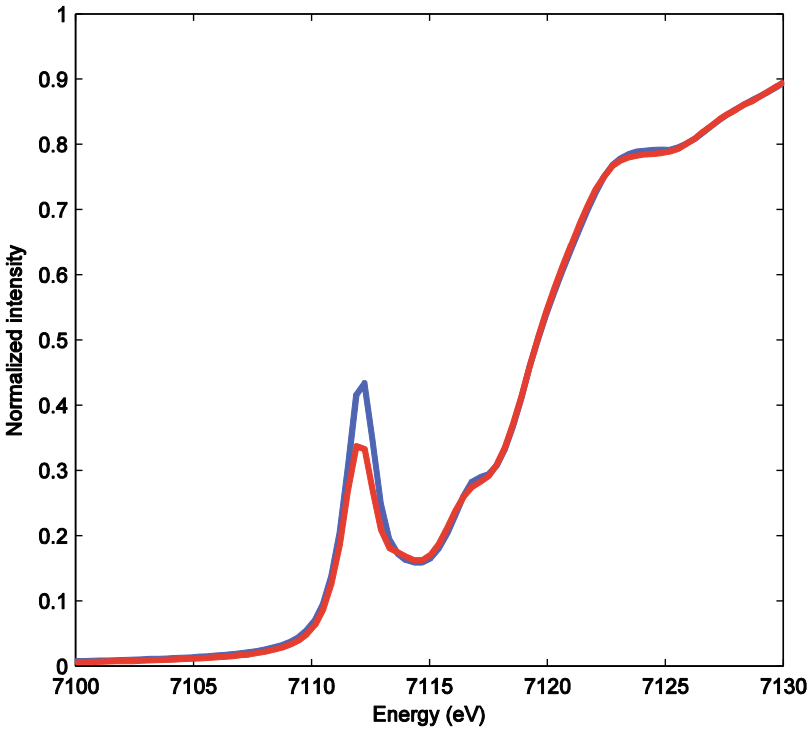


**Fig. S37.**

Pre-edge region of the XANES spectrum of the sample of $[(P_3^B)Fe{\equiv}N]^+$ for the first set of scans (blue) and the second set of scans (red), showing evidence of photodamage.

**Table S1.**

X-ray diffraction data and structure refinement details for $(P_3^B)Fe(NNMe_2)$ and $(P_3^B)Fe(OTf)$

| | $(P_3^B)Fe(NNMe_2)$ | $(P_3^B)Fe(OTf)$ |
|---|---|---|
| **Identification code** | nbt_3_14_final | nbt_2_275_final |
| **Empirical formula** | C38 H60 B Fe N2 P3 | C37 H54 B F3 Fe O3 P3 S |
| **Formula weight** | 704.45 | 795.43 |
| **Temperature** | 100(2) K | 100(2) K |
| **Wavelength** | 0.71073 Å | 0.71073 Å |
| **Crystal system** | Triclinic | Monoclinic |
| **Space group** | P-1 | $P2_1/c$ |
| **Unit cell dimensions** | a = 10.6719(10) Å α= 91.269(3)°. | a = 10.8053(4) Å α= 90°. |
| | b = 10.7538(9) Å β= 91.242(4)°. | b = 14.9993(5) Å β= 92.4740(10)°. |
| | c = 16.3248(16) Å γ = 104.316(3)°. | c = 24.4155(9) Å γ = 90°. |
| **Volume** | 1814.2(3) $Å^3$ | 3953.4(2) $Å^3$ |
| **Z** | 2 | 4 |
| **Density (calculated)** | 1.290 $Mg/m^3$ | 1.336 $Mg/m^3$ |
| **Absorption coefficient** | 0.578 $mm^{-1}$ | 0.604 $mm^{-1}$ |
| **F(000)** | 756 | 1676 |
| **Crystal size** | 0.120 x 0.110 x 0.060 $mm^3$ | .1 x .1 x .1 $mm^3$ |
| **Theta range for data collection** | 2.712 to 28.282°. | 2.442 to 38.334°. |
| **Index ranges** | -14<=h<=14, -14<=k<=14, -21<=l<=21 | -18<=h<=18, -26<=k<=26, -42<=l<=42 |
| **Reflections collected** | 69829 | 334561 |
| **Independent reflections** | 9018 [R(int) = 0.0429] | 21954 [R(int) = 0.0510] |
| **Completeness to theta = 25.242°** | 99.9 % | 99.9 % |
| **Absorption correction** | Semi-empirical from equivalents | Semi-empirical from equivalents |
| **Refinement method** | Full-matrix least-squares on $F^2$ | Full-matrix least-squares on $F^2$ |
| **Data / restraints / parameters** | 9018 / 9 / 500 | 21954 / 0 / 454 |
| **Goodness-of-fit on $F^2$** | 1.040 | 1.042 |
| **Final R indices [I>2sigma(I)]** | R1 = 0.0591, wR2 = 0.1509 | R1 = 0.0354, wR2 = 0.0790 |
| **R indices (all data)** | R1 = 0.0712, wR2 = 0.1587 | R1 = 0.0503, wR2 = 0.0844 |
| **Extinction coefficient** | n/a | n/a |
| **Largest diff. peak and hole** | 2.463 and -1.309 e.$Å^{-3}$ | 0.924 and -1.286 e.$Å^{-3}$ |

**Table S2.**

Mössbauer simulation parameters for the spectra shown in Fig. S20.

| Component | δ (mm $s^{-1}$) | $\|\Delta E_Q\|$ (mm $s^{-1}$) | Γ (mm $s^{-1}$) | Rel. area |
|---|---|---|---|---|
| | | **Spectrum A** | | |
| 1 ($(P_3^B)Fe(NNH_2)$) | 0.14 | 1.63 | 0.41 | 0.89 |
| 2 ($[(P_3^B)FeN_2]^{2-}$) | 0.26 | 0.82 | 0.57 | 0.07 |
| 3 | 1.09 | 2.01 | 0.76 | 0.09 |
| | | **Spectrum B** | | |
| 1 ($[(P_3^B)Fe{\equiv}N]^+$) | −0.15 | 6.20 | 0.32 | 0.47 |
| 2 ($(P_3^B)Fe(NNH_2)$) | 0.14 | 1.63 | 0.38 | 0.12 |
| 3 | 0.01 | 1.46 | 0.50 | 0.16 |
| 4 | 0.61 | 1.43 | 0.64 | 0.09 |
| 5 | 0.80 | 2.32 | 0.65 | 0.24 |
| 1 ($[(P_3^B)Fe{\equiv}N]^+$) (Mask) | −0.15 | 6.20 | 0.32 | 0.48 |
| | | **Spectrum C** | | |
| 1 ($[(P_3B)Fe{\equiv}N]^+$) | −0.15 | 6.20 | 0.35 | 0.56 |
| 2 | 0.09 | 1.08 | 0.64 | 0.30 |
| 3 | 0.47 | 1.76 | 0.71 | 0.20 |
| 4 | 0.73 | 2.39 | 0.38 | 0.07 |
| 1 ($[(P_3^B)Fe{\equiv}N]^+$) (Mask) | −0.15 | 6.20 | 0.35 | 0.57 |

**Table S3.**

Mössbauer simulation parameters for the spectra shown in Fig. S21.

| Component | δ (mm $s^{-1}$) | $\lvert\Delta E_Q\rvert$ (mm $s^{-1}$) | Γ (mm $s^{-1}$) | Rel. area |
|---|---|---|---|---|
| | | **Spectrum A** | | |
| 1 (($P_3^B$)Fe($NNH_2$)) | 0.14 | 1.63 | 0.43 | 0.91 |
| 2 ([($P_3^B$)$FeN_2$]$^{2-}$) | 0.26 | 0.82 | 0.46 | 0.09 |
| 3 | 0.78 | 2.48 | 0.35 | 0.03 |
| | | **Spectrum B** | | |
| 1 ([($P_3^B$)Fe≡N]$^+$) | −0.15 | 6.20 | 0.37 | 0.22 |
| 2 | 0.03 | 1.49 | 0.61 | 0.39 |
| 3 | 0.06 | 0.93 | 0.41 | 0.15 |
| 4 | 0.83 | 1.19 | 0.53 | 0.09 |
| 5 | 0.70 | 2.36 | 0.84 | 0.20 |
| 1 ([($P_3^B$)Fe≡N]$^+$) (Mask) | −0.15 | 6.20 | 0.39 | 0.24 |

**Table S4.**

Mössbauer simulation parameters for the spectra shown in Fig. S24.

| Component | δ (mm $s^{-1}$) | $\|\Delta E_Q\|$ (mm $s^{-1}$) | Γ (mm $s^{-1}$) | Rel. area |
|---|---|---|---|---|
| | | **Spectrum A** | | |
| 1 ($[(P_3^B)Fe{\equiv}N]^+$) | −0.15 | 6.20 | 0.47 | 0.58 |
| 2 ($(P_3^B)Fe(NNH_2)$) | 0.14 | 1.63 | 0.55 | 0.18 |
| 3 | 0.03 | 1.20 | 0.70 | 0.18 |
| 4 | 0.79 | 2.22 | 0.68 | 0.24 |
| 1 ($[(P_3^B)Fe{\equiv}N]^+$) (Mask) | −0.15 | 6.20 | −0.50[a] | 0.49 |
| | | **Spectrum B** | | |
| 1 ($(P_3^B)Fe(OTf)$)[b] | 0.68 | 2.53 | 0.32 | 0.42 |
| 2 | 1.47 | 3.83 | 0.32 | 0.42 |
| 3 | 0.92 | 3.75 | 0.49 | 0.14 |
| 4 | 0.97 | 2.02 | 0.39 | 0.07 |

[a]In this case, a pseudo-Voigt line shape was found to provide a superior fit to the masked data. The pseudo-Voigt is given by the convolution of a Gaussian function of linewidth 0.50 mm $s^{-1}$ with a Lorentzian function of intrinsic Mössbauer linewidth (0.19 mm $s^{-1}$). This line shape reflects a distribution of quadrupole splittings in the sample arising from inhomogeneity, e.g. from partial crystallization of the 2-MeTHF. [b]The best-fit parameters for this species are, within typical experimental error, identical to that of $(P_3^B)Fe(OTf)$. However, the parameters are also quite similar to $[(P_3^B)Fe][BAr^F{}_4]$ (Table S15), so the slight deviation may be due to $[(P_3^B)Fe][OTf]$, i.e. outer-sphere versus inner-sphere $OTf^-$.

**Table S5.**

Mössbauer simulation parameters for the spectra shown in Fig. S25.

| Component | $\delta$ (mm s$^{-1}$) | $\lvert\Delta E_Q\rvert$ (mm s$^{-1}$) | $\Gamma$ (mm s$^{-1}$) | Rel. area |
|---|---|---|---|---|
| | | **Spectrum A** | | |
| 1 (($P_3^B$)Fe($NNH_2$))[a] | 0.14 ± 0.03 | 1.54 ± 0.1 | 0.45 | 0.80 |
| 2 ([($P_3^B$)Fe$N_2$]$^{2-}$)[a] | 0.24 ± 0.03 | 0.97 ± 0.1 | 0.51 | 0.21 |
| 3 | 0.72 | 2.31 | 0.36 | 0.08 |
| | | **Spectrum B** | | |
| 1 ([($P_3^B$)Fe≡N]$^+$) | −0.15 | 6.20 | 0.35 | 0.56 |
| 2 | 0.09 | 1.08 | 0.64 | 0.30 |
| 3 | 0.47 | 1.76 | 0.71 | 0.20 |
| 4 | 0.73 | 2.39 | 0.38 | 0.07 |
| 1 ([($P_3^B$)Fe≡N]$^+$) (Mask) | −0.15 | 6.20 | 0.35 | 0.57 |

[a]The additional broad component in the baseline (species 3) was simulated by a symmetric quadrupole doublet with Lorentzian line shape, but an examination of the residual shows that this only approximates the true sub-spectrum, possibly due to magnetic hyperfine splitting. Accordingly, the uncertainty in the simulated parameters for the first two components is increased, estimated to be $\sigma = \pm 0.03$ mm s$^{-1}$ in $\delta$ and $\sigma = \pm 0.1$ mm s$^{-1}$ in $\lvert\Delta E_Q\rvert$ from a Monte Carlo simulation of the error in counting statistics.

**Table S6.**

Pre-edge XANES fitting parameters (Figs. S26–S29).

**Figure S26 ($(P_3^B)Fe(NNMe_2)$)**

**Baseline**

| *Amplitude* | *Position (eV)* | *FWHM (eV)* | *Mixing* | *Offset* | *Slope* | *Twist* |
|---|---|---|---|---|---|---|
| 8.98 | 7123.89 | 0.14 | 0 | −0.29 | −0.009 | 0.0008 |

**Components**

| | *Amplitude* | *Position (eV)* | *FWHM (eV)* | *Mixing* | *LW-ratio* |
|---|---|---|---|---|---|
| **1** | 0.06 | 7111.39 | 0.88 | 0 | – |
| **2** | 0.10 | 7115.49 | 1.11 | 0 | – |

**Figure S27 ($(P_3^B)Fe(NNH_2)$)**

**Baseline**

| *Amplitude* | *Position (eV)* | *FWHM (eV)* | *Mixing* | *Offset* | *Slope* | *Twist* |
|---|---|---|---|---|---|---|
| 0.38 | 7118.73 | 0.66 | 0 | −0.1 | 0.03 | 0.003 |

**Components**

| | *Amplitude* | *Position (eV)* | *FWHM (eV)* | *Mixing* | *LW-ratio* |
|---|---|---|---|---|---|
| **1** | 0.05 | 7111.62 | 0.82 | 0.43 | 0.94 |
| **2** | 0.04 | 7115.91 | 0.74 | 1 | 1 |

**Figure S28 ($[(P_3^B)Fe{\equiv}N]^+$)**

**Baseline**

| *Amplitude* | *Position (eV)* | *FWHM (eV)* | *Mixing* | *Offset* | *Slope* | *Twist* |
|---|---|---|---|---|---|---|
| 0.56 | 7118.97 | 1.46 | 0.68 | 0.06 | 0.02 | 0.002 |

**Components**

| | *Amplitude* | *Position (eV)* | *FWHM (eV)* | *Mixing* | *LW-ratio* |
|---|---|---|---|---|---|
| **1** | 0.40 | 7112.09 | 0.79 | 0.09 | 1.07 |
| **2** | 0.02 | 7114.27 | 1.07 | 1 | 0.80 |
| **3** | 0.08 | 7116.66 | 0.87 | 1 | 1.07 |

**Figure S29 ($[(P_3^B)FeN_2]^{2-}$)**

**Baseline**

| *Amplitude* | *Position (eV)* | *FWHM (eV)* | *Mixing* | *Offset* | *Slope* | *Twist* |
|---|---|---|---|---|---|---|
| 10.16 | 7137.66 | 9.15 | 0 | −11.79 | −0.42 | −0.01 |

**Components**

| | *Amplitude* | *Position (eV)* | *FWHM (eV)* | *Mixing* | *LW-ratio* |
|---|---|---|---|---|---|
| **1** | 0.04 | 7112.58 | 1.23 | 0 | – |
| **2** | 0.09 | 7114.37 | 1.19 | 0 | – |

**Table S7.**

EXAFS fitting parameters for $(P_3^B)Fe(NNMe_2)$. The final simulation is highlighted in grey.

| Shell | N | R (Å) | $\sigma^2$ (Å$^2$) | $E_0$ (eV) | $F^a$ | Red. $\chi^{2\,b}$ |
|---|---|---|---|---|---|---|
| | | | ***Simulation 1*** | | | |
| N | 1 | 1.652(4) | 0.0024(4) | | | |
| P | 3 | 2.233(2) | 0.0025(1) | −11.4(6) | 0.248 | 0.673 |
| | | | ***Simulation 2*** | | | |
| N | 1 | 1.654(4) | 0.0024(4) | | | |
| P | 3 | 2.229(3) | 0.0026(1) | | | |
| B | 1 | 2.44(3) | 0.005(4) | −12.6(8) | 0.248 | 0.679 |
| | | | ***Simulation 3***$^c$ | | | |
| N | 1 | 1.655(4) | 0.0025(3) | | | |
| P | 3 | 2.231(2) | 0.0026(1) | | | |
| B | 1 | 2.43(3) | 0.007(6) | | | |
| C | 3 | 3.367(8) | 0.0023(6) | −12.0(5) | 0.229 | 0.584 |
| | | | ***Simulation 4*** | | | |
| N | 1 | 1.654(2) | 0.0022(2) | | | |
| P | 3 | 2.232(1) | 0.0027(1) | | | |
| B | 1 | 2.49(2) | 0.007(2) | | | |
| N—N | 2 | 2.997(3) | 0.0020(2) | | | |
| C1 | 3 | 3.31(2) | 0.010(5) | | | |
| C2 | 3 | 3.38(1) | 0.0030(7) | −11.7(5) | **0.127** | **0.184** |

[a]The F-factor (goodness-of-fit) is given by: $\boldsymbol{F} = \left[\frac{\sum \boldsymbol{k^6}(\chi_{expt}-\chi_{calc})^2}{\sum \boldsymbol{k^6}\chi^2_{expt}}\right]^{\frac{1}{2}}$. [b]The reduced $\chi^2$ is given by $\boldsymbol{\chi^2} = \frac{\boldsymbol{F}}{(\boldsymbol{N}-\boldsymbol{p})}$ where $N$ is the number of experimental data points, and $p$ is the number of parameters refined in least-squares fitting. [c]Attempting to include a second C-atom scatterer in this simulation produced an unphysically short distance of ~3.1 Å. Thus only a single C-scatterer was considered.

**Table S8.**

EXAFS fitting parameters for $(P_3^B)Fe(NNH_2)$. The final simulation is highlighted in grey.

| Shell | N | R (Å) | $\sigma^2$ (Å$^2$) | $E_0$ (eV) | $F^a$ | Red. $\chi^{2\,b}$ |
|---|---|---|---|---|---|---|
| | | | ***Simulation 1*** | | | |
| N | 1 | 1.653(4) | 0.0042(4) | | | |
| P | 3 | 2.229(2) | 0.0042(1) | −13.8(6) | 0.258 | 0.383 |
| | | | ***Simulation 2*** | | | |
| N | 1 | 1.654(4) | 0.0044(4) | | | |
| P | 3 | 2.232(2) | 0.0042(1) | | | |
| B | 1 | 2.79(1) | 0.002(1) | −13.2(6) | 0.242 | 0.340 |
| | | | ***Simulation 3***$^c$ | | | |
| N | 1 | 1.655(4) | 0.0044(4) | | | |
| P | 3 | 2.234(2) | 0.0042(1) | | | |
| B | 1 | 2.787(8) | 0.0014(8) | | | |
| C | 3 | 3.349(6) | 0.0030(6) | −12.4(6) | 0.228 | 0.305 |
| | | | ***Simulation 4*** | | | |
| N | 1 | 1.654(3) | 0.0043(3) | | | |
| P | 3 | 2.233(2) | 0.0042(1) | | | |
| B | 1 | 2.79(4) | 0.006(4) | | | |
| N—N | 2 | 2.99(1) | 0.008(1) | | | |
| C1 | 3 | 3.350(6) | 0.0031(5) | | | |
| C2 | 3 | 3.67(2) | 0.011(3) | −12.8(6) | **0.196** | **0.228** |
| | | | ***Simulation 5***$^d$ | | | |
| N | 1 | 1.656(4) | 0.0058(5) | | | |
| P | 3 | 2.239(1) | 0.0044(1) | | | |
| N—N | 2 | 2.995(7) | 0.0070(7) | | | |
| C | 3 | 3.343(8) | 0.0044(8) | −11.5(5) | 0.168 | 0.171 |

$^a$The F-factor (goodness-of-fit) is given by: $\boldsymbol{F} = \left[\frac{\sum \boldsymbol{k^6}(\chi_{expt}-\chi_{calc})^2}{\sum \boldsymbol{k^6}\chi^2_{expt}}\right]^{\frac{1}{2}}$. $^b$The reduced $\chi^2$ is given by $\boldsymbol{\chi^2} = \frac{\boldsymbol{F}}{(\boldsymbol{N}-\boldsymbol{p})}$ where $N$ is the number of experimental data points, and $p$ is the number of parameters refined in least-squares fitting. $^c$Attempting to include a second C-atom scatterer in this simulation produced an unphysically short distance of ~3.1 Å. Thus only a single C-scatterer was considered. $^d$The simulation was performed over $k$ = 2–12 Å$^{-1}$.

**Table S9.**

EXAFS fitting parameters for $[(P_3^B)Fe{\equiv}N]^+$. The final simulation is highlighted in grey.

| Shell | N | R (Å) | $\sigma^2$ (Å$^2$) | $E_0$ (eV) | $F^a$ | Red. $\chi^{2\,b}$ |
|---|---|---|---|---|---|---|
| | | | ***Simulation 1*** | | | |
| N | 1 | 1.544(5) | 0.0061(6) | | | |
| P | 3 | 2.255(2) | 0.0043(1) | −12.5(6) | 0.255 | 0.381 |
| | | | ***Simulation 2*** | | | |
| N | 1 | 1.545(5) | 0.0061(5) | | | |
| P | 3 | 2.256(2) | 0.0042(1) | | | |
| B | 1 | 2.77(1) | 0.0015(9) | −12.1(6) | 0.242 | 0.340 |
| | | | ***Simulation 3*** | | | |
| N | 1 | 1.546(3) | 0.0060(4) | | | |
| P | 3 | 2.257(1) | 0.0042(1) | | | |
| B | 1 | 2.770(6) | 0.0008(5) | | | |
| C1 | 3 | 3.352(5) | 0.0029(4) | | | |
| C2 | 3 | 3.711(9) | 0.0045(9) | −11.9(5) | 0.174 | 0.183 |
| | | | ***Simulation 4***$^c$ | | | |
| N | 1 | 1.541(3) | 0.0057(3) | | | |
| P | 3 | 2.249(2) | 0.0047(1) | | | |
| B | 1 | 2.751(7) | 0.0010(5) | | | |
| C1 | 3 | 3.322(5) | 0.0028(4) | | | |
| C2 | 3 | 3.677(6) | 0.0028(5) | −17.6(6) | **0.170** | **0.174** |
| | | | ***Simulation 5***$^d$ | | | |
| N | 1 | 1.548(3) | 0.0066(4) | | | |
| P | 3 | 2.258(1) | 0.0038(1) | | | |
| B | 1 | 2.72(1) | 0.003(1) | | | |
| C1 | 3 | 3.351(4) | 0.0009(3) | | | |
| C2 | 3 | 3.73(1) | 0.008(2) | −11.6(6) | 0.130 | 0.119 |
| | | | ***Simulation 6***$^e$ | | | |
| N | 1 | 1.551(3) | 0.0053(4) | | | |
| P | 3 | 2.243(2) | 0.0045(1) | | | |
| B | 1 | 2.75(2) | 0.005(2) | | | |
| C1 | 3 | 3.328(4) | 0.0019(3) | | | |
| C2 | 3 | 3.653(6) | 0.0023(5) | −18.1(6) | 0.180 | 0.202 |

[a]The F-factor (goodness-of-fit) is given by: $\boldsymbol{F} = \left[\frac{\sum \boldsymbol{k^6}(\chi_{expt}-\chi_{calc})^2}{\sum \boldsymbol{k^6}\chi^2_{expt}}\right]^{\frac{1}{2}}$. [b]The reduced $\chi^2$ is given by $\boldsymbol{\chi^2} = \frac{\boldsymbol{F}}{(\boldsymbol{N}-\boldsymbol{p})}$ where $N$ is the number of experimental data points, and $p$ is the number of parameters refined in least-squares fitting. [c]The *ab initio* single-scattering Fe–N and Fe–P phase and amplitude functions were re-calculated from the optimized distances obtained in Simulation 3. [d]The simulation was performed over $k$ = 2–12 Å$^{-1}$. [e]Data from the set of second scans, showing evidence for photodamage (Fig. S37), were simulated using the same model as simulation 4.

**Table S10.**

EXAFS fitting parameters for $[(P_3^B)FeN_2]^{2-}$. The final simulation is highlighted in grey.

| Shell | N | R (Å) | $\sigma^2$ (Å$^2$) | $E_0$ (eV) | $F^a$ | Red. $\chi^{2\,b}$ |
|---|---|---|---|---|---|---|
| | | | ***Simulation 1*** | | | |
| N | 1 | 1.774(4) | 0.0006(3) | | | |
| P | 3 | 2.183(3) | 0.0025(1) | −11.2(9) | 0.344 | 1.389 |
| | | | ***Simulation 2*** | | | |
| N | 1 | 1.775(3) | 0.0005(2) | | | |
| P | 3 | 2.181(2) | 0.0026(1) | | | |
| N—N | 2 | 2.937(3) | 0.0009(2) | | | |
| C1 | 6 | 3.221(8) | 0.0064(9) | | | |
| C2 | 3 | 3.67(2) | 0.006(2) | −11.7(5) | **0.223** | **0.601** |

[a]The F-factor (goodness-of-fit) is given by: $\boldsymbol{F} = \left[\frac{\sum \boldsymbol{k^6}(\chi_{expt}-\chi_{calc})^2}{\sum \boldsymbol{k^6}\chi^2_{expt}}\right]^{\frac{1}{2}}$. [b]The reduced $\chi^2$ is given by $\boldsymbol{\chi^2} = \frac{\boldsymbol{F}}{(\boldsymbol{N}-\boldsymbol{p})}$ where $N$ is the number of experimental data points, and $p$ is the number of parameters refined in least-squares fitting.

**Table S11.**

$NH_3/N_2H_4$ quantification results from low temperature protonation of $[(P_3^B)FeN_2]^{2-}$ and $[Na(12\text{-crown-}4)_2][(P_3^B)Fe(N_2)]$, as well as the result of a catalytic reaction using $[(P_3^B)Fe][BAr^F{}_4]$ as a precursor. Yields are with respect to Fe.

| Run | Fe precursor | Equiv. TfOH | Equiv. $CoCp^*_2$ | % yield $NH_3$ | % yield $N_2H_4$ |
|---|---|---|---|---|---|
| 1 | $[(P_3^B)FeN_2]^{2-}$ | 20 | 0 | 36 | n.d. |
| 2 | $[(P_3^B)FeN_2]^{2-}$ | 20 | 0 | 37 | n.d. |
| Avg. | | | | 36.0(5) | – |
| 1 | $[(P_3^B)FeN_2]^{2-}$ | 20 | 10 | 85 | n.d. |
| 2 | $[(P_3^B)FeN_2]^{2-}$ | 20 | 10 | 61 | n.d. |
| Avg. | | | | 73(17) | – |
| 1 | $[(P_3^B)Fe(N_2)]$ $[Na(12\text{-crown-}4)_2]$ | 20 | 0 | 36 | 9 |
| 2 | $[(P_3^B)Fe(N_2)]$ $[Na(12\text{-crown-}4)_2]$ | 20 | 0 | 32 | 10 |
| Avg. | | | | 34(3) | 9(1) |
| | | ***Catalytic reaction*** | | | |
| 1 | $[(P_3^B)Fe][BAr^F{}_4]$ | 107 | 54 | 654 | n.d. |

**Table S12.**

Best fit parameters of variable temperature NMR data of $(P_3^B)Fe(NNMe_2)$ to equation (1). The 95% confidence interval is given in brackets below each parameter.

| $g_p$ | Resonance | ΔH (kcal mol$^{-1}$) | ΔS (cal mol$^{-1}$ K$^{-1}$) | $\delta_d$ (ppm) | $C$ (K$^{-1}$ × 10$^6$) |
|---|---|---|---|---|---|
| 3 | *N*-C<u>H</u>$_3$ | 3.62<br>[3.26, 3.98] | -0.457<br>[-38.9, 38.0] | 2.16<br>[1.65, 2.68] | -1.27<br>[-25.0, 22.5] |
| 3 | P | 3.80<br>[3.72, 3.89] | 3.50<br>[1.67, 5.32] | 110<br>[106, 114] | 8.11<br>[1.90, 14.3] |
| | **Avg.** | 3.7(1) | 2(3) | | |
| 5 | *N*-C<u>H</u>$_3$ | 3.62<br>[3.26, 3.98] | -1.37<br>[-38.0, 35.3] | 2.16<br>[1.64, 2.67] | -1.21<br>[-22.8, 20.4] |
| 5 | P | 3.77<br>[3.70, 3.84] | 1.78<br>[-0.265, 3.82] | 109<br>[106, 112] | 11.0<br>[1.14, 20.8] |
| | **Avg.** | 3.7(1) | 0(2) | | |

**Table S13.**

Gas-phase optimized core structures of the ground state of $(P_3^B)Fe(NNMe_2)$ ($S = 0$) using a variety of pure functionals

| | XRD | BP86 | ZORA-BP86 | M06-L | TPSS |
|---|---|---|---|---|---|
| d(Fe–$N_\alpha$) (Å) | 1.680 | 1.673 | 1.671 | 1.664 | 1.675 |
| d(Fe–B) (Å) | 2.534 | 2.554 | 2.564 | 2.478 | 2.499 |
| d(Fe–P1) (Å) | 2.267 | 2.307 | 2.304 | 2.277 | 2.310 |
| d(Fe–P2) (Å) | 2.247 | 2.224 | 2.231 | 2.190 | 2.227 |
| d(Fe–P3) (Å) | 2.239 | 2.244 | 2.251 | 2.230 | 2.247 |
| d($N_\alpha$–$N_\beta$) (Å) | 1.293 | 1.303 | 1.309 | 1.300 | 1.302 |
| ∡(P2FeP3) (°) | 109.9 | 108.6 | 108.9 | 108.5 | 108.4 |
| ∡(P1FeP3) (°) | 104.3 | 104.4 | 104.7 | 109.0 | 103.0 |
| ∡(P1FeP2) (°) | 125.8 | 127.0 | 126.5 | 124.6 | 129.1 |
| ∡(BFe$N_\alpha$) (°) | 168.9 | 166.9 | 167.9 | 169.9 | 165.7 |
| Mean Error (%)[a] | — | 0.828 | 0.755 | 1.44 | 1.26 |

[a]The mean error is calculated as the mean value of $|p_{exp} - p_{calc}|/p_{exp}$ for each parameter $p$ in the table, multiplied by 100.

**Table S14.**

Gas-phase energy differences (ΔH and ΔS) for $(P_3^B)Fe(NNMe_2)$ as a function of spin state using a variety of pure functionals.

| | **BP86** | **ZORA-BP86** | **M06-L** | **TPSS** |
|---|---|---|---|---|
| ΔH (*S* = 0) (kcal mol$^{-1}$) | 0 | 0 | 0 | 0 |
| ΔH (*S* = 1) (kcal mol$^{-1}$) | 4.05 | 3.13 | −7.36 | 1.99 |
| ΔH (*S* = 2) (kcal mol$^{-1}$) | 28.5 | 26.7 | 12.1 | 25.1 |
| ΔS (*S* = 0) (cal mol$^{-1}$ K$^{-1}$) | 0 | 0 | 0 | 0 |
| ΔS (*S* = 1) (cal mol$^{-1}$ K$^{-1}$) | 8.22 | 8.79 | 6.78 | 9.46 |
| ΔS (*S* = 2) (cal mol$^{-1}$ K$^{-1}$) | 15.0 | 10.7 | 10.7 | 16.0 |

**Table S15.**

Experimental and computed Mössbauer parameters used to calibrate the DFT method.

| | $\delta_{exp}$ (mm $s^{-1}$) | $\delta_{calc}$[a] (mm $s^{-1}$) | $\rho(0)$ (a.u.$^{-3}$) | $\lvert\Delta E_{Q,exp}\rvert$ (mm $s^{-1}$) | $\lvert\Delta E_{Q,calc}\rvert$ (mm $s^{-1}$) |
|---|---|---|---|---|---|
| $[(P_3^B)Fe(NH_3)]^+$ [b] | 0.68 | 0.71 | 11819.48535 | 1.94 | 2.13 |
| $[(P_3^B)Fe(N_2H_4)]^+$ [b] | 0.70 | 0.68 | 11819.56915 | 2.30 | 2.06 |
| $(P_3^B)Fe(NH_2)$ [b] | 0.60 | 0.52 | 11819.96313 | 1.47 | 1.57 |
| $(P_3^B)Fe(OTf)$ | 0.71 | 0.71 | 11819.48664 | 2.62 | 2.32 |
| $[(P_3^B)Fe(N_2)]^-$ [b] | 0.40 | 0.40 | 11820.24712 | 0.99 | 0.82 |
| $[(P_3^B)Fe(NAd)]^+$ [b] | 0.15 | 0.12 | 11820.95795 | 1.31 | 1.17 |
| $(P_3^B)Fe(NNMe_2)$ | 0.17 | 0.22 | 11820.70707 | 1.73 | 2.04 |
| $(P_3^B)Fe(NAd)$ [b] | 0.04 | 0.09 | 11821.02742 | 1.40 | 1.56 |
| $(PhBP_3^{iPr})Fe{\equiv}N$ [c] | −0.34 | −0.36 | 11822.13478 | 6.01 | 5.51 |
| **RMSD** | | 0.04 | | | 0.3 |

[a]Isomer shifts were calculated according to the equation $\delta_{calc} = \alpha(\rho(0) - C) + \beta$, with $\alpha = -0.407$ mm $s^{-1}$ a.u.$^3$, $\beta = 4.575$ mm $s^{-1}$, and $C = 11810$ a.u.$^{-3}$. The constants were determined from a least squares linear regression of $\delta_{exp}$ versus $\rho(0) - C$ ($r^2 = 0.99$). [b]Parameters taken from.[4] [c]Parameters taken from.[20]

**Table S16.**

Calculated gas-phase energy differences (ΔH and ΔS) and spectroscopic parameters for $(P_3^B)Fe(NNH_2)$ and $[(P_3^B)Fe{\equiv}N]^+$ as a function of spin state.

| | ***S* = 0** | ***S* = 1** | ***S* = 2** |
|---|---|---|---|
| $(P_3^B)Fe(NNH_2)$ | | | |
| ΔH (kcal $mol^{-1}$) | 0 | 1.80 | 23.9 |
| ΔS (cal $mol^{-1}$ $K^{-1}$) | 0 | 3.79 | 1.17 |
| $\delta_{calc}$ (mm $s^{-1}$) | 0.19(4) | 0.46(4) | 0.56(4) |
| $\lvert\Delta E_{Q,calc}\rvert$ (mm $s^{-1}$) | 1.7(3) | 0.7(3) | 1.1(3) |
| $[(P_3^B)Fe{\equiv}N]^+$ | | | |
| ΔH (kcal $mol^{-1}$) | 0 | 7.58 | 34.2 |
| ΔS (cal $mol^{-1}$ $K^{-1}$) | 0 | 5.57 | 12.2 |
| $\delta_{calc}$ (mm $s^{-1}$) | −0.21(4) | −0.23(4) | 0.01(4) |
| $\lvert\Delta E_{Q,calc}\rvert$ (mm $s^{-1}$) | 5.6(3) | 1.4(3) | 2.5(3) |

**Table S17.**

Comparison of the gas-phase optimized core structures of $[(P_3^B)Fe{\equiv}N]^+$ ($S$ = 0) and $(P_3^B)Fe{\equiv}N$ ($S$ = 1/2).

| | **$[(P_3^B)Fe{\equiv}N]^+$** | **$(P_3^B)Fe{\equiv}N$** |
|---|---|---|
| d(Fe–N) (Å) | 1.514 | 1.549 |
| d(Fe–B) (Å) | 2.954 | 2.702 |
| d(Fe–P1) (Å) | 2.315 | 2.274 |
| d(Fe–P2) (Å) | 2.305 | 2.271 |
| d(Fe–P3) (Å) | 2.292 | 2.253 |
| ∡(P2FeP3) (°) | 108.4 | 109.3 |
| ∡(P1FeP3) (°) | 115.6 | 116.1 |
| ∡(P1FeP2) (°) | 122.4 | 121.5 |
| ∡(BFeN) (°) | 175.5 | 176.2 |

**Supplementary Acknowledgements**

We would like to thank L. Henling and M. Takase for assistance with XRD, D. VanderVelde for assistance with NMR, and T. J. Del Castillo for assistance with catalytic experiments. The SSRL Structural Molecular Biology Program is supported by the DOE Office of Biological and Environmental Research, and by the National Institutes of Health, National Institute of General Medical Sciences (including P41GM103393). The contents of this publication are solely the responsibility of the authors and do not necessarily represent the official views of NIGMS or NIH.

**References**

1. Bontemps, S.; Bouhadir, G.; Dyer, P. W.; Miqueu, K.; Bourissou, D. *Inorg. Chem.* **2007,** *46*, 5149-5151.
2. Moret, M.-E.; Peters, J. C. *Angew. Chem. Int. Ed.* **2011,** *50*, 2063-2067.
3. Anderson, J. S.; Moret, M. E.; Peters, J. C. *J. Am. Chem. Soc.* **2013,** *135*, 534-537.
4. Del Castillo, T. J.; Thompson, N. B.; Peters, J. C. *J. Am. Chem. Soc.* **2016,** *138*, 5341-5350.
5. Berto, T. C.; Hoffman, M. B.; Murata, Y.; Landenberger, K. B.; Alp, E. E.; Zhao, J.; Lehnert, N. *J. Am. Chem. Soc.* **2011,** *133*, 16714-16717.
6. Sheldrick, G. *Acta Crystallogr. A* **2015,** *71*, 3-8.
7. Sheldrick, G. *Acta Crystallogr. C* **2015,** *71*, 3-8.
8. I. Prisecaru, WMOSS4 Mössbauer Spectral Analysis Software, www.wmoss.org, 2009-2016.
9. G. N. George, I. J. Pickering, EXAFSPAK: A suite of computer programs for analysis of X-ray absorption spectra. SSRL, Stanford. (1995).
10. Rehr, J. J.; Kas, J. J.; Vila, F. D.; Prange, M. P.; Jorissen, K. *Phys. Chem. Chem. Phys.* **2010,** *12*, 5503-5513.
11. Neese, F. *Wiley Interdisciplinary Reviews: Computational Molecular Science* **2012,** *2*, 73-78.
12. (a) Becke, A. D. *Phys. Rev. A* **1988,** *38*, 3098-3100; (b) Perdew, J. P. *Phys. Rev. B* **1986,** *33*, 8822-8824.
13. Zhao, Y.; Truhlar, D. G. *J. Chem. Phys.* **2006,** *125*, 194101.
14. Tao, J.; Perdew, J. P.; Staroverov, V. N.; Scuseria, G. E. *Phys. Rev. Lett.* **2003,** *91*, 146401.
15. Weigend, F.; Ahlrichs, R. *Phys. Chem. Chem. Phys.* **2005,** *7*, 3297-3305.
16. van Wüllen, C. *J. Chem. Phys.* **1998,** *109*, 392-399.
17. Pantazis, D. A.; Chen, X.-Y.; Landis, C. R.; Neese, F. *J. Chem. Theory Comput.* **2008,** *4*, 908-919.
18. Staroverov, V. N.; Scuseria, G. E.; Tao, J.; Perdew, J. P. *J. Chem. Phys.* **2003,** *119*, 12129-12137.
19. Neese, F. *Inorg. Chim. Acta* **2002,** *337*, 181-192.
20. Hendrich, M. P.; Gunderson, W.; Behan, R. K.; Green, M. T.; Mehn, M. P.; Betley, T. A.; Lu, C. C.; Peters, J. C. *Proc. Nat. Acad. Sci.* **2006,** *103*, 17107-17112.

21. Rohde, J.-U.; Betley, T. A.; Jackson, T. A.; Saouma, C. T.; Peters, J. C.; Que, L., Jr. *Inorg. Chem.* **2007,** *46*, 5720-5726.
22. Rittle, J.; Peters, J. C. *J. Am. Chem. Soc.* **2016,** *138*, 4243-4248.
23. George, S. J.; Fu, J. X.; Guo, Y. S.; Drury, O. B.; Friedrich, S.; Rauchfuss, T.; Volkers, P. I.; Peters, J. C.; Scott, V.; Brown, S. D.; Thomas, C. M.; Cramer, S. P. *Inorg. Chim. Acta* **2008,** *361*, 1157-1165.